Remote Sensing of Environment 280 (2022) 113211

Contents lists available at ScienceDirect

Remote Sensing of Environment

journal homepage: www.elsevier.com/locate/rse

Multispectral discrimination of spectrally similar hydrothermal minerals in mafic crust: A 5000 km^2 ASTER alteration map of the Oman–UAE ophiolite

Thomas M. Belgrano [a,b,*], Larryn W. Diamond [b], Nevena Novakovic [b], Robert D. Hewson [c], Christoph A. Hecker [c], Robin C. Wolf [b], Ludwik de Doliwa Zieliński [b], Raphael Kuhn [b], Samuel A. Gilgen [b]

[a] School of Ocean and Earth Science, National Oceanography Centre Southampton, University of Southampton, Southampton SO14 3ZH, UK
[b] Institute of Geological Sciences, University of Bern, Baltzerstrasse 3, 3012 Bern, Switzerland
[c] Department of Applied Earth Sciences, Faculty of Geo-Information Science and Earth Observation, University of Twente, Enschede, 7500 AE, the Netherlands

ARTICLE INFO

Edited by Jing M. Chen

Keywords:
ASTER
Oman
Ophiolite
VMS
Mafic
Hydrothermal
Alteration
Multispectral

ABSTRACT

Multispectral remote sensing of hydrothermal alteration in volcanogenic massive sulfide (VMS) ore systems in mafic crust is relatively uncommon, in part due to the short-wave infrared spectral similarity of several key alteration minerals: epidote, chlorite, actinolite, and serpentine. In this study, we developed regional mosaic generation and classification workflows for Advanced Spaceborne Thermal Emission and Reflection Radiometer (ASTER) imagery to discriminate these minerals over the entire crust of the Semail ophiolite (Oman–UAE). Spectral discrimination was achieved through adaptation of the ASTER (pre-)processing workflow to the specific mapping targets, available datasets, and location of this study. Necessary steps included the pre-selection of ASTER scenes without residual atmospheric water features, mosaic normalization based solely on overlapping target outcrops, correcting cross-mosaic ramp errors, and alteration map classification based on image-derived reference data. The resulting alteration map, validated through comparison with field mapping and sampling, is the most areally extensive continuous survey of hydrothermal alteration yet presented for oceanic crust, providing a renewed framework for research and mineral exploration of Earth's largest ophiolite. Our map confirms that the vast majority of the upper oceanic crust is regionally altered to a spilite type secondary mineral assemblage. Localized areas of epidosite alteration, marking focused hydrothermal flow paths, are confined to the upper oceanic crust, whereas areas of previously unrecognized but intense actinolite alteration are common in both the lower and upper oceanic crust. Our methodological developments expand the standard considerations necessary for regional geological mapping using infrared image mosaics. They further demonstrate the under-appreciated capability of multispectral data for mapping spectrally similar rock types. Although the specifics of the method are necessarily optimized for the Oman–UAE ophiolite, re-optimization based on local reference data should allow similar results to be achieved in other well-exposed mafic-hosted VMS districts.

1. Introduction

Remote sensing is routinely applied to the mapping of hydrothermal alteration related to magmatic–hydrothermal ore systems (e.g., Mars and Rowan, 2006; van der Meer et al., 2012) as well as to certain classes of seafloor black-smoker type volcanogenic massive sulfide (VMS) ore systems (e.g., Hewson et al., 2005; van der Meer et al., 2012). However, successful remote sensing of hydrothermal alteration associated with VMS deposits in mafic volcanic terranes, classified after Barrie and Hannington (1997), is uncommon, despite the deposits being important sources of Cu, Zn, and Au (e.g., Jowitt et al., 2005; Rajendran and Nasir, 2017). This is partly due to the similar shortwave infrared (SWIR) reflectance spectra of common key alteration minerals: chlorite, epidote, actinolite, and serpentine (e.g., Abweny et al., 2016; Dalton et al., 2004), especially in multispectral data. Many of these alteration minerals are common to mafic-hosted VMS systems across tectonic settings and geological time, including modern seafloor massive sulfide deposits, Phanerozoic ophiolites, and Archean greenstone belts (Galley et al.,

* Corresponding author at: School of Ocean and Earth Science, National Oceanography Centre Southampton, University of Southampton, Southampton SO14 3ZH, UK.
E-mail address: T.Belgrano@soton.ac.uk (T.M. Belgrano).

https://doi.org/10.1016/j.rse.2022.113211
Received 6 January 2022; Received in revised form 24 July 2022; Accepted 30 July 2022
Available online 17 August 2022

2007). Variations in the abundances of these minerals can mark different segments of the fossil fluid-flow patterns that generated the deposits (Galley et al., 2007). An improved ability to identify the presence and geometry of such patterns would help mineral explorers to assess the VMS prospectivity of different areas and vector towards concealed ore deposits (Jowitt et al., 2005).

Methods for processing multispectral imagery into geological maps are typically developed for standardized reapplication to different case studies with spectrally similar minerals often necessarily lumped together (e.g., Kalinowski et al., 2004; Rowan and Mars, 2003; van der Meer et al., 2012). Less explored are the capabilities of multispectral data processed with highly case-study-optimized workflows. These may extend the routine utility of multispectral imagery, such as Advanced Spaceborne Thermal Emission and Reflection Radiometer (ASTER), to the mapping of mafic-dominated VMS systems.

In the following, we develop an ASTER processing method to regionally discriminate hydrothermally altered rocks characterized by the spectrally similar minerals epidote, chlorite, actinolite, and serpentine across most of the oceanic crust exposed in the Semail ophiolite (Oman–UAE). Such discrimination, generally considered intractable with ASTER and challenging even with hyperspectral imagery (Dalton et al., 2004; Hewson et al., 2005; Rowan and Mars, 2003), was achieved by adding new (pre-)processing steps to established workflows and by rigorously optimizing each step to the targets and surface conditions specific to this study.

1.1. Previous remote sensing studies of the Semail ophiolite

Pioneering studies in the Semail ophiolite demonstrated the utility of multispectral Landsat imagery for mapping the main ophiolite lithologies and also Fe-oxide and undifferentiated chlorite and epidote alteration (e.g., Abrams et al., 1988; Rothery, 1984). Multispectral infrared ASTER imagery has been collected since 1999, and has since been applied to mapping lithologies and alteration in the Semail ophiolite in the mantle, mantle transition zone, and around VMS deposits (e.g., Rajendran and Nasir, 2019, 2017). A HyMap™ airborne hyperspectral survey has also been used to map ophiolite lithologies via characteristic primary and secondary mineralogy in the Tayin block (Roy et al., 2009). Collectively, these studies demonstrate the versatility of infrared remote sensing and the excellent conditions for such studies over the arid and sparsely vegetated Arabian Peninsula.

1.2. Geological framework and surface conditions

The Semail ophiolite, exposed over ~17,000 km^2 across northern Oman and the U.A.E. (Fig. 1a), is a nappe of Cretaceous oceanic lithosphere tectonically emplaced onto the Arabian margin (Lippard et al., 1986). The ophiolite is domed into a gentle anticline, exposing a 30–50° E–NE dipping oblique crustal section along its north-eastern flank. This crustal section has a pseudo-stratigraphic thickness of ~6–9 km (Fig. 1b), and an along-strike continuity of ~300 km along the Batinah Plain (Lippard et al., 1986; Nicolas et al., 2000). The volcanic sequence along the Batinah Plain also hosts ~14 known VMS deposits (Gilgen et al., 2014), and as such, exposes an entire VMS mineral system for study and exploration.

The axial crust of the Semail ophiolite, comprising much of the lower crustal gabbros, the overlying sheeted dyke complex (SDC) and the Geotimes basal volcanic unit, was formed at an oceanic spreading axis in a supra-subduction zone, potentially proto-arc tectonic setting (Belgrano and Diamond, 2019; MacLeod et al., 2013). Hydrous Lasail unit basalts

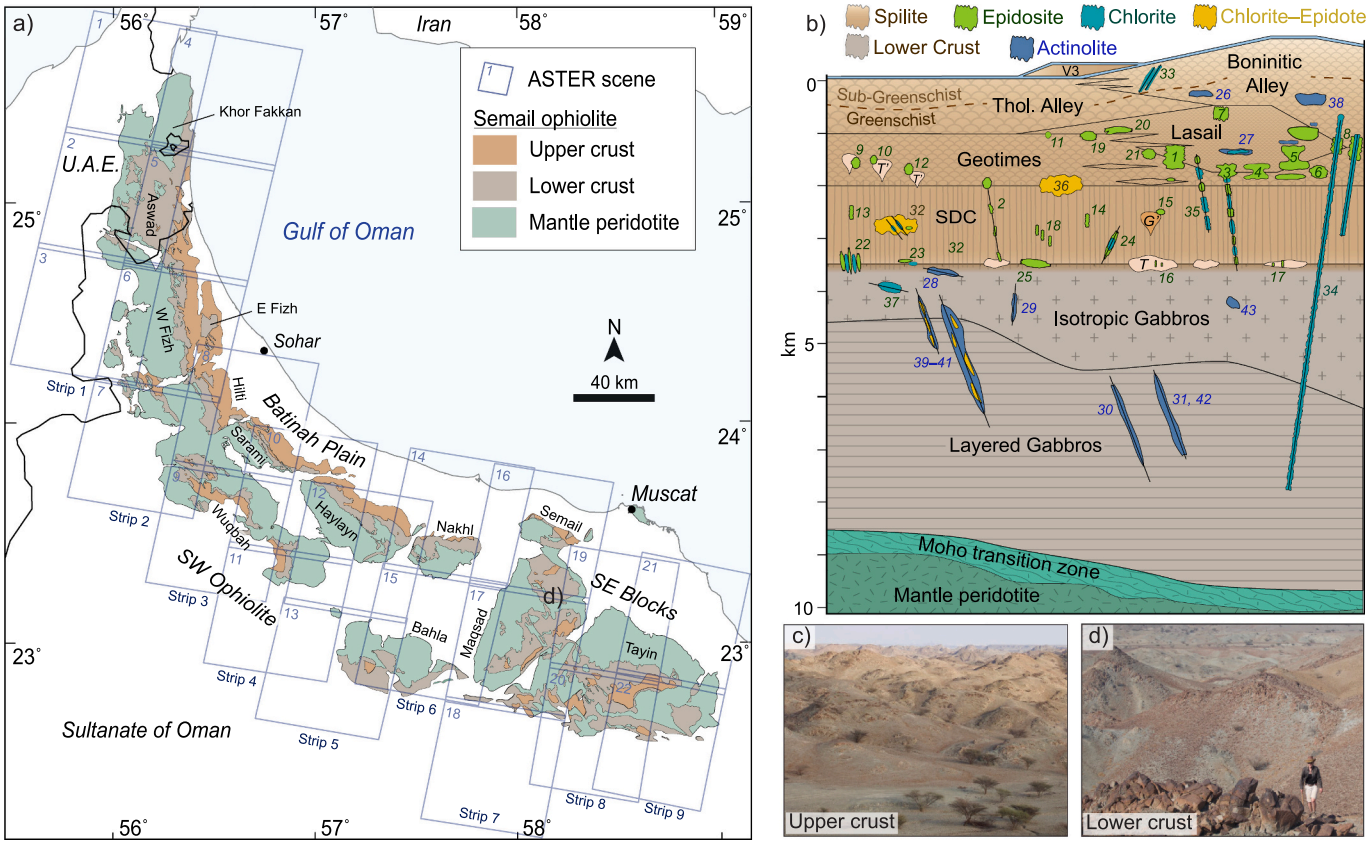

Fig. 1. a) Map of the Semail ophiolite study area and the 22 ASTER scenes and nine orbital swaths used in this study, numbered in correspondance to Table S2. b) Crustal pseudo-stratigraphy of the Semail ophiolite with the positions of 43 confirmed localized alteration zones (Table A1; Belgrano et al., 2022). Unit thicknesses are approximate (Belgrano et al., 2019; Lippard et al., 1986). c) Typical well-exposed outcrop conditions for the upper crustal dykes and lavas. d) Typical outcrop conditions for the lower crustal gabbros.

were locally erupted both on- and off-axis, and this entire sequence was buried by post-axial Tholeiitic Alley unit and Boninitic Alley unit lavas (Belgrano et al., 2019). This post-axial volcanism was accompanied by comagmatic intrusion of wehrlites, gabbros, tonalites, and trondhjemites throughout the Semail crust (Lippard et al., 1986).

The Semail ophiolite crustal outcrops targeted for remote sensing have a mean elevation of 510 ± 255 m (1σ) above sea level and flank the higher elevation Hajar mountains (up to 3000 m). Due to this relatively low target elevation and the situation of the study area on the semi- to hyper-arid Arabian Peninsula, mean annual rainfall is <200 mm/yr over the targeted outcrops (Charabi and Al-Yahyai, 2013). Vegetation is accordingly extremely sparse, covering no more than a few percent of the outcropping rock surfaces (e.g., Fig. 1c, d). More vegetation exists within wadis (beds of ephemeral rivers), which needs to be masked or taken into account by remote sensing studies.

2. Data, software, and analytical methods

Field mapping was conducted in Oman using GPS-guided tablets between 2012 and 2020. Mineral identification in the field was supported by SWIR spectroscopy with a PIMA II (Portable Infrared Mineral Analyser; Integrated Spectronics Pty Ltd.). Alteration mineralogy was further assessed at the University of Bern by routine thin-section microscopy, Raman spectroscopy using a Horiba Scientific LABRAM HR-800, and powder X-ray diffraction (XRD) using a PANalytical CubiX3 diffractometer. Details of the XRD method are given in the supplement.

Further infrared reflectance spectra were collected using an Analytical Spectral Devices (ASD) FieldSpec 3 (Malvern Panalytical Ltd.) at the University of Twente, from 350 to 2500 nm, with 1 nm sampling and calibrated between every sample with Spectralon™ corrected for its reflectance properties. Thermal infrared (TIR) spectra were measured using a Bruker Vertex 70 TIR spectrophotometer at the University of Twente according to Hecker et al. (2011). Owing to the low (90 m) spatial resolution of the ASTER TIR bands, the TIR spectra were ultimately not used, but are provided in Fig. S2 for future work.

Level 1 ASTER L1T (V003) precision terrane and crosstalk corrected granules were downloaded in 2018 from the NASA Earth Explorer platform (NASA LP DAAC, 2015). ASTER has three forward looking visible to near infrared (VNIR) bands with 15 m pixel size: b1 (0.52–0.60 μm), b2 (0.63–0.69 μm), and b3 (0.76–0.86 μm); six shortwave infrared (SWIR) bands with 30 m pixel size: b4 (1.600–1.700 μm), b5 (2.145–2.185 μm), b6 (2.185–2.225), b7 (2.235–2.285 μm), b8 (2.295–2.365), b9 (2.360–2.430); and five thermal infrared (TIR) bands with 90 m pixels (Table S1; NASA LP DAAC, 2015). Twenty-two L1T granules were selected (Fig. 1a) and processed in ENVI™ 5.5 software (L3Harris Technologies, Inc.), then exported to QGIS™ 3.2 (www.qgis.org) and Adobe Illustrator™ (Adobe Inc.) software for final map production. Table S2 lists the 22 ASTER granule IDs and their acquisition parameters.

3. Field and petrological descriptions of alteration types

Pervasive hydrothermal alteration has been described, to some extent, at all structural levels in the Semail crust (Alabaster and Pearce, 1985; Greenberger et al., 2021; Kelemen et al., 2020; Nehlig and Juteau, 1988; Pflumio, 1991; Stakes and Taylor, 1992). Below we review and describe the petrological and outcrop characteristics most important to the task of remotely mapping the target hydrothermal alteration types, based primarily on samples and observations collected in the Northern and Central ophiolite blocks.

3.1. Regional spilite and lower crustal alteration

3.1.1. Upper crust

Spilite type alteration pervades the vast majority of the upper crust of the Semail ophiolite, and hence constitutes the 'regional' alteration (Alabaster and Pearce, 1985; Pflumio, 1991) from which the other more spatially localized alteration types need to be discriminated. Spilite secondary mineralogy in the SDC consists of sub-greenschist to greenschist-facies assemblages of albite, chlorite, Fe-oxide, titanite ± actinolite ± epidote ± quartz (see also Alabaster and Pearce, 1985; Pflumio, 1991). Relict primary minerals typically include clinopyroxene, incompletely albitized plagioclase and titanomagnetite (Alabaster and Pearce, 1985; Belgrano et al., 2019; Pflumio, 1991). Partially epidotised dykes occur sporadically, cumulatively making up less than a few vol% of regionally altered outcrop. The dyke rocks generally only develop a patchy thin orange weathering patina, rather than a thick rind or desert varnish, and are otherwise well exposed for remote sensing.

The Geotimes and overlying Lasail lava units are also pervasively altered to spilite assemblages comparable to the SDC, but usually without actinolite (Fig. 2a; see also Alabaster and Pearce, 1985; Pflumio, 1991). Geotimes spilites characteristically develop a thin hematitic weathering patina. Lasail unit spilites mostly only develop patchy, very thin orange weathering patinas. Sporadic patches and nodules of epidosite are present in most areas of otherwise spilitic regional alteration in Geotimes and Lasail lavas, cumulatively making up only a few vol% of the outcrop.

The upper Alley group volcanic units are typically pervasively altered to a sub-greenschist secondary mineralogy of albite + chlorite + interlayered chlorite–smectite + clay + quartz or chalcedony + Fe-oxide ± titanite (Belgrano et al., 2019; Pflumio, 1991). Other common secondary minerals are celadonite, zeolites, Fe^{3+}-pumpellyite, prehnite, and calcite. Thick weathering rinds tend not to form on the surfaces of the Alley volcanic units.

3.1.2. Lower crust

Clinopyroxenes in the top few tens of meters of gabbro beneath the SDC are often pervasively recrystallised to hornblende, which are in turn usually partially altered to actinolite (Fig. S3a; Nehlig and Juteau, 1988). Characterization of hydrothermal alteration below this thin layer of pervasive recrystallization is a topic of ongoing research; however, secondary hornblende, chlorite, serpentine, and prehnite are common constituents of the regional lower crustal gabbro alteration (Greenberger et al., 2021; Stakes and Taylor, 1992). More intense alteration occurs in the vicinity of faults and shear zones, manifested by hornblende, actinolite, chlorite, epidote, prehnite, zeolites, and calcite (Coogan et al., 2006; Greenberger et al., 2021; Kelemen et al., 2020; Nehlig and Juteau, 1988). Outcrop exposure in the lower crustal units is generally good, but the terrane is steeper than in the upper crust, and the weathered surfaces tend to develop thick Fe-oxide weathering rinds (e.g., Fig. 1d).

3.2. Localized alteration types

In addition to the regionally extensive alteration described above, several mineralogically distinct types of intense, pervasive hydrothermal alteration are present as localized bodies. At their highest intensities, these localized alteration types may completely overprint magmatic and precursor spilite mineralogy and textures with an assemblage of just a few minerals. The positions of previously and newly documented important sites of localized alteration are illustrated in Fig. 1b and listed in Table A1 (Belgrano et al., 2022).

3.2.1. Epidosite

Alteration to endmember epidosite produces granoblastic rocks consisting of epidote + quartz + minor titanite and Fe-oxides (Gilgen et al., 2016; Weber et al., 2021). At the outcrop scale, epidotisation develops differently through the different upper-crustal lithologies. In pillow lavas, epidotization often begins in the interpillows, progresses to the pillow cores, then finally the pillow rims, forming completely epidotized pillow stacks (e.g., Fig. 2b; Gilgen et al., 2016). In massive lavas, intermediate epidosite alteration is often confined to the margins of

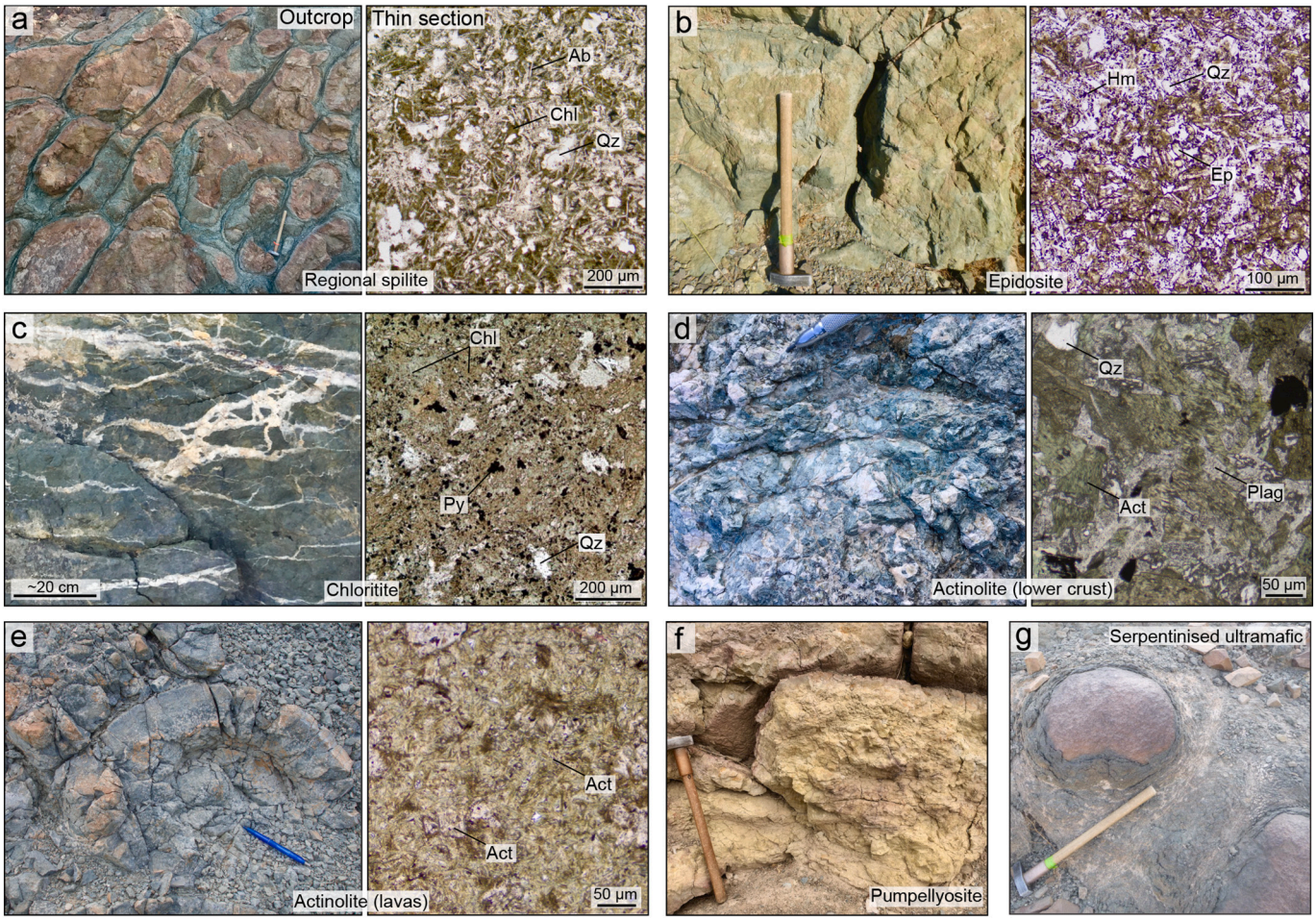

Fig. 2. Field and plane-polarised thin-section photographs of common alteration types in the Semail ophiolite crust. a) Typical spilite alteration of Geotimes basaltic-andesite pillow lavas. b) Complete epidosite alteration of Geotimes pillow lavas. c) Chloritite alteration around quartz veins. d) Partially actinolite-altered gabbro near a fault zone in the lower crust. e) Pervasive actinolite alteration of Boninitic Alley pillow lavas. f) Pumpellyosite in Boninitic Alley pillow lavas. g) Serpentinized upper crustal ultramafic intrusion with onion-skin weathering.

cooling joints, whereas in dykes it follows primary textural banding, resulting in striped alteration along the dyke cores (Gilgen et al., 2016). Epidosites generally form good exposures for remote sensing, but can have thick Fe-oxide rinds on old, weathered surfaces.

3.2.2. *Chloritite and chlorite–epidote alteration*

The mineral chlorite is present as a constituent of the regional alteration throughout much of the Semail crust (Fig. 2a; Alabaster and Pearce, 1985; Stakes and Taylor, 1992). Localized chloritite alteration to rocks consisting almost entirely of chlorite ± quartz ± sulfides is far less common, but has been described in three distinct situations in the ophiolite. Firstly, chloritites occur within the stockwork zones directly beneath VMS deposits (A'Shaikh et al., 2006), secondly, as massive bodies in lower crustal gabbros and the SDC (Miyashita and Adachi, 2020; Yoshitake et al., 2009), and thirdly, as alteration haloes bordering late, probably obduction-related quartz–hematite veins (Fig. 2c; Belgrano et al., 2019). Intensely chloritised outcrops are generally dark in visible and VNIR wavelengths, have high Fe contents (Belgrano et al., 2019; Miyashita and Adachi, 2020), and hence often develop thick Fe-oxide weathering rinds.

During this study, several zones of mixed chlorite–epidote alteration were identified by ASTER in the upper crust. In some cases, this alteration type can be cryptic and difficult to recognize in the field, but elevated chlorite and epidote contents may be revealed by careful hand lens, XRD or SWIR analysis.

3.2.3. *Actinolite alteration*

The study area includes two main types of localized, intense actinolite alteration in the ophiolite crust. In the lower crust, blueish grey, coarse-grained actinolite occurs as an alteration product of hornblende in hornblende-rich rocks and as pervasive alteration haloes along lower crustal fault zones (Fig. 2d). Localized, pervasive actinolite alteration also occurs in primitive lavas of the Lasail and Boninitic Alley volcanic units (Fig. 2e). This alteration is difficult to recognize in outcrop, as the individual actinolite crystals are very fine or microscopic, but often imparts a blueish–grey colour to lavas which otherwise typically alter to pale greenish-grey spilites (Fig. 2e). In thin section, this actinolite is colourless to light green and forms fibrous aggregates of crystals (Fig. 2e). Outcrops altered to actinolite in both the lower and upper crust tend not to form thick weathering rinds.

3.2.4. *Pumpellyosites*

Pods a few meters in extent of pervasive pumpellyosite alteration (Fe^{3+}-pumpellyite ± quartz ± hematite) are widespread in the Alley volcanic units and occasionally present in the Geotimes lavas (Belgrano et al., 2019; Pflumio, 1991). Pumpellyosites are dull mustard yellow to olive green (Fig. 2f). Massive pumpellyite alteration occasionally extends over larger areas, up to 100 s of meters across. The weathered surfaces of pumpellyosite locally develop Fe-oxide rinds.

3.2.5. *Serpentinized ultramafic intrusions*

Ultramafic intrusions in the Semail crust, mainly wehrlites, dunites,

and mixed peridotite and gabbro, are all serpentinized to some extent (BRGM, 1993; Lippard et al., 1986). Serpentinites were not a target of this study, but serpentine minerals are spectrally similar to the target minerals at the ASTER band resolution, and it was therefore necessary to discriminate them from other alteration types. Serpentinized ultramafic outcrops generally display low albedo with well-developed Fe-oxide weathering rinds (Fig. 2g).

4. ASTER pre-processing method

To map these different alteration types, we generated a spectrally consistent ASTER mosaic of the entire ophiolite crust, corrected it to surface reflectance, and classified it based on image data extracted over field-mapped reference sites. This workflow (Fig. 3) is largely synthesized and adapted from the processing steps described by Du et al. (2001), Hewson et al. (2005), Mars and Rowan (2006), and Cudahy et al. (2020).

4.1. Scene selection

Initial attempts at selecting the minimum number of cloud-free ASTER scenes needed to cover the study area yielded mosaics with residual normalization errors following spectral normalization, which prevented regionally consistent discrimination of the spectrally similar target rock types. We identified both variable geometric and atmospheric effects during acquisition as the causes of this inconsistency, and this could be mitigated through scene selection from the ASTER archive.

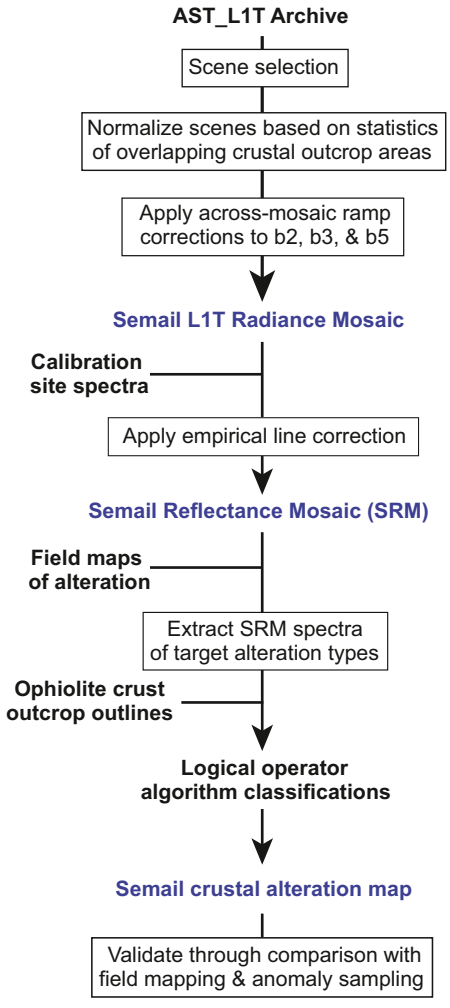

Fig. 3. Flowchart of ASTER processing steps required to generate a reliable alteration map of spectrally similar alteration types in the Semail ophiolite, largely synthesized and adapted from Du et al. (2001), Hewson et al. (2005), Mars and Rowan (2006), and Cudahy et al. (2020).

4.1.1. Acquisition geometry

Shadowed areas are disproportionately affected by crosstalk from the ASTER b4 sensor onto b5 and b9 (Mars and Rowan, 2006). Band ratios involving b5 and b9, crucial for our study, may therefore be inconsistent between differently shaded images of the same area. To minimize this effect as well as any other inconsistencies related to acquisition geometry, scenes were selected for their similar acquisition geometries. Acquisitions for 19 out of 22 scenes have solar azimuths of 119–130°N and solar elevation angles of 63–69°. Only Strip 1 has slightly outlying solar azimuths of 090–094° and elevation angles of 73–74°, however, overlain by Strip 2 it covers very little of the mapped area (Fig. 1a, Table S2).

4.1.2. Screening of scenes for residual atmospheric water features

Despite working with cloud-free ASTER scenes, transient atmospheric features detectable in bands 7–9 (2.2–2.43 μm) are present in many ASTER archive scenes over the ophiolite. These features are front-like, dividing the scene into two domains (Fig. 4). These features are probably related to atmospheric moisture as they depress b7, b8, and particularly b9 (2.43 μm), located on the edge of an atmospheric water vapor absorption wavelength region (Hewson et al., 2005). Two examples of these features are shown in Fig. 4, visible as a shift in the overall hue of the scene towards yellow moving from the SW to NE and marked by a dashed red line. The presence of such residual atmospheric features across overlapping image areas prevented accurate normalization of bands 7–9, which are crucial for discriminating the target alteration types. Our solution was to download all available scenes with acceptable acquisition geometries (Section 4.1.1), batch process band 7, 8, 9 images, apply an equalization stretch, and retain only the scenes where the ophiolite crust was free of these features (e.g., Fig. 4a). Such fronts are common, and half of the considered scenes were discarded at this stage.

4.2. Spectral normalization into a consistent mosaic

Following this careful scene selection, 22 ASTER scenes collected along nine swaths remained to cover the study area (Fig. 1a). Each swath consists of an orbital strip of 2–4 consecutively acquired scenes that are spatially and spectrally consistent with one another except for bad edge pixels which needed to be masked (Fig. 4a). The geolocation of ASTER L1T is accurate enough that no spatial co-registration of the different strips was necessary (Section 6.1). However, spectral normalization between strips was necessary and was performed consecutively from one strip to another, from Strip 1 to 9 (Fig. 5). This normalization was achieved using the equations for band gains and offsets described in Eq. (2) in Du et al. (2001), as reproduced below:

$$gain\ (i_2) = \frac{\sigma_{\,i\ 1B}}{\sigma_{\,i\ 2A}} \tag{1}$$

$$offset\ (i_2) = \mu_{\,i\ 1B} - \frac{\sigma_{\,i\ 1B}}{\sigma_{\,i\ 2A}} \times \mu_{\,i\ 2A} \tag{2}$$

For example, to normalize Strip 2 to reference Strip 1, gains (Eq. (1)) and offsets (Eq. (2)) are applied to each band (i) of Strip 2, determined from the means (μ) and standard deviations (σ) of select areas of overlapping pixels. These select areas, A and B, are on the eastern side of the reference strip and the western side of the strip to be adjusted, respectively.

Typically, the greatest possible number of suitable overlapping pixels between two scenes is used to calculate μ and σ, optimizing for scene-wide normalization accuracy (Du et al., 2001; Hewson et al., 2005). The target crustal outcrops along the Batinah Plain are flanked to the SW by high mountains and to the NE by seasonally vegetated and mobile wadis and gravel terraces. Initial attempts to include these flanking

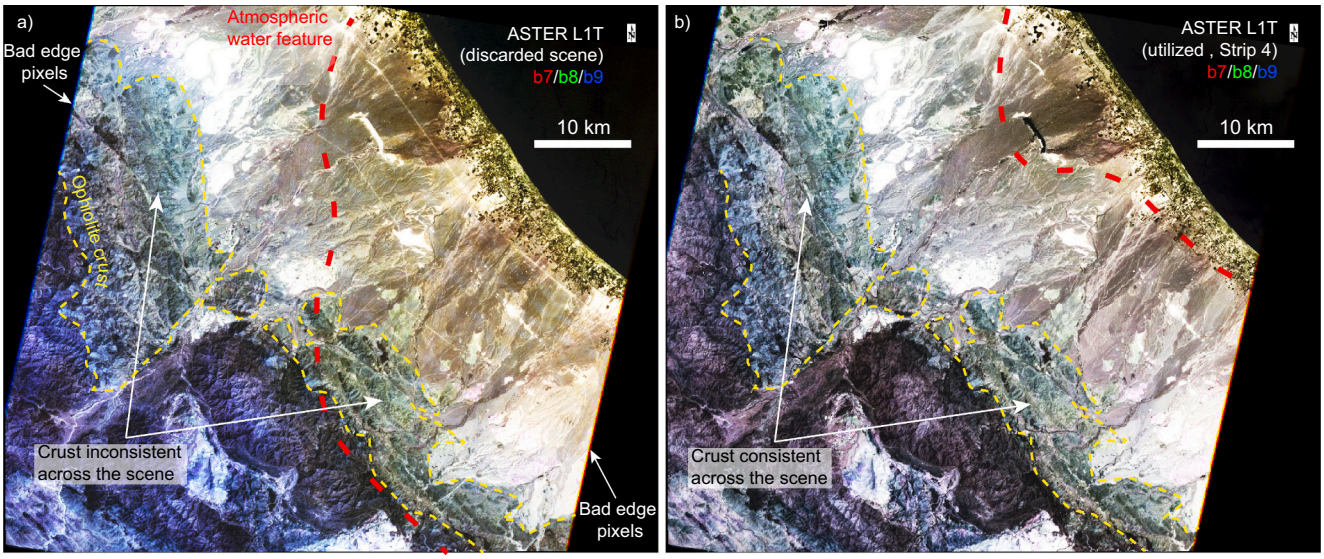

Fig. 4. Examples of ASTER L1T b7,8,9 radiance images showing residual atmospheric water features that subdivide scenes (along red dashed lines) and prevent accurate mosaic normalization. a) Discarded scene in which these features overlap the target strip of crustal outcrops (yellow dashed outline). b) Scene without this overlap, accepted for normalization. (For interpretation of the references to colour in this figure legend, the reader is referred to the web version of this article.)

areas for calculating normalization statistics resulted in residual normalization errors over the target outcrops. We effectively eliminated these residual errors by selecting overlapping pixels exclusively from the areas of targeted ophiolite crustal outcrop running through the centre of the mosaic. In the Semail Gap (Fig. 5c), where ophiolite rocks are absent, other areas of outcrop at similar altitude were used for this purpose (Fig. 5a, c). These overlapping outcrop areas (Fig. 5b) were manually drawn with the aid of L1T VNIR imagery and geological maps. With overlapping areas thus defined, the strips were converted to floating point format to avoid resolution loss associated with multiplying integer data (Du et al., 2001) and normalized in sequence. The normalization statistics and overlapping area Shapefiles are provided in the data archive (Belgrano et al., 2022). The effectiveness of this normalization is demonstrated by the absence of visible seamlines through the target crustal outcrops (Fig. 5d) and confirmed by the lack of stepped band ratios at scene boundaries (Fig. 6).

4.3. Correcting across-mosaic ramp errors

Cudahy et al. (2020) documented a detector-array calibration error in ASTER L1T b5, perpendicular to the swath and inducing a ~ 2% fade across each scene. This is additive in mosaics merging several adjacent strips by overlapping edge normalization, and results in across-mosaic ramp errors. Adapting the approach of Cudahy et al. (2020), we constructed a spectral transect through the crustal outcrops on the north-eastern side of the ophiolite, excluding non-ophiolite segments, and plotted b5/b6 and b7/b6 radiance ratios against km East (Figs. 5c, 6). As in Cudahy et al. (2020), b5/b6 decreased from W to E, amounting to an ~8% reduction in b5 over nine adjacent strips (Fig. 6b). Contrastingly, the linear regression for b6/b7 is flat, demonstrating the suitability of b6 as a well-calibrated reference band and of the transect itself for correcting this b5 ramp error (Fig. 6a). We inverted the initial b5/b6 linear regression slope (*m* in Fig. 6) into an E–W linear ramp image using the ENVI™ 'generate test data' tool, starting with a value of 1 on its western side, as the westernmost strip was not adjusted during mosaic normalization. We then multiplied the b5 mosaic with this ramp image (Cudahy et al., 2020), resulting in a flat b5/b6 regression along the transect (green line in Fig. 6b).

We also discovered across-mosaic positive ramp errors in b2 and b3 radiance relative to b1, which if ignored lead to apparent NW–SE differences in vegetation and Fe-oxide indices as well as in our alteration classifications. From NW to SE, b2 radiance increased by ~4% over the extent of the mosaic, whereas b3 increased by ~10% (Fig. 6c). In our field observations (e.g., Belgrano et al., 2019), there are no substantial differences in outcrop vegetation or Fe-oxide abundance along the length of the ophiolite that could explain these slopes. The flat b4/b1 transect further rules out a natural increase in Fe-oxide abundance and demonstrates that b1 is a well-calibrated reference band (Fig. 6a). As such, b2/b1 and b3/b1 linear regressions were also used to derive corrective ramps and applied to the mosaic as for b5 (Fig. 6c). The success of these three corrections is demonstrated by the consistent band ratio image and flat spectral transect regressions across the mosaic (Figs. 5d, 6b–c.).

4.4. Empirical line calibration to reflectance

Following this normalization and ramp correction, we applied a single empirical line calibration (ELC) to the entire normalized mosaic, using one bright and one dark calibration target, to convert L1T radiance to estimated surface reflectance (Smith and Milton, 1999). Details of the ELC targets are summarised below and in Table S4, together with the dates of high-resolution imagery used to confirm the state of the targets around the time of ASTER acquisition.

For the dark target, we used an area of black plastic sheeting covering mine waste (Fig. 7a). During sampling in 2018 this sheeting contained large gaps and was dusty in places (Fig. 7a). In the ASTER scene acquired in April 2006, however, the plastic appears intact and spectrally homogeneous. High resolution OrbView-3 imagery acquired in January 2007, the nearest time available, supports this, showing that the utilized NE portion of the sheeting was intact and relatively free of dust within 8 months of the ASTER acquisition (Fig. 7c). On this basis, we assume that our samples of the plastic sheeting are representative of the 2006 surface captured by ASTER (Fig. 7b). Both the ASTER L1T and ASD FieldSpec3 spectra of the sheeting are of low reflectance and homogeneous (Fig. 7e–f). The apparently high b1 and b2 for both the dark and bright targets in the L1T spectra are due to ASTER acquisition under 'High Gain' mode for VNIR b1–b3 versus 'Normal Gain' mode for the SWIR b4–b9. However, as each band is regressed and corrected independently, this has no significant effect on the ELC result.

For the bright target, we used the tops of two limestone blocks

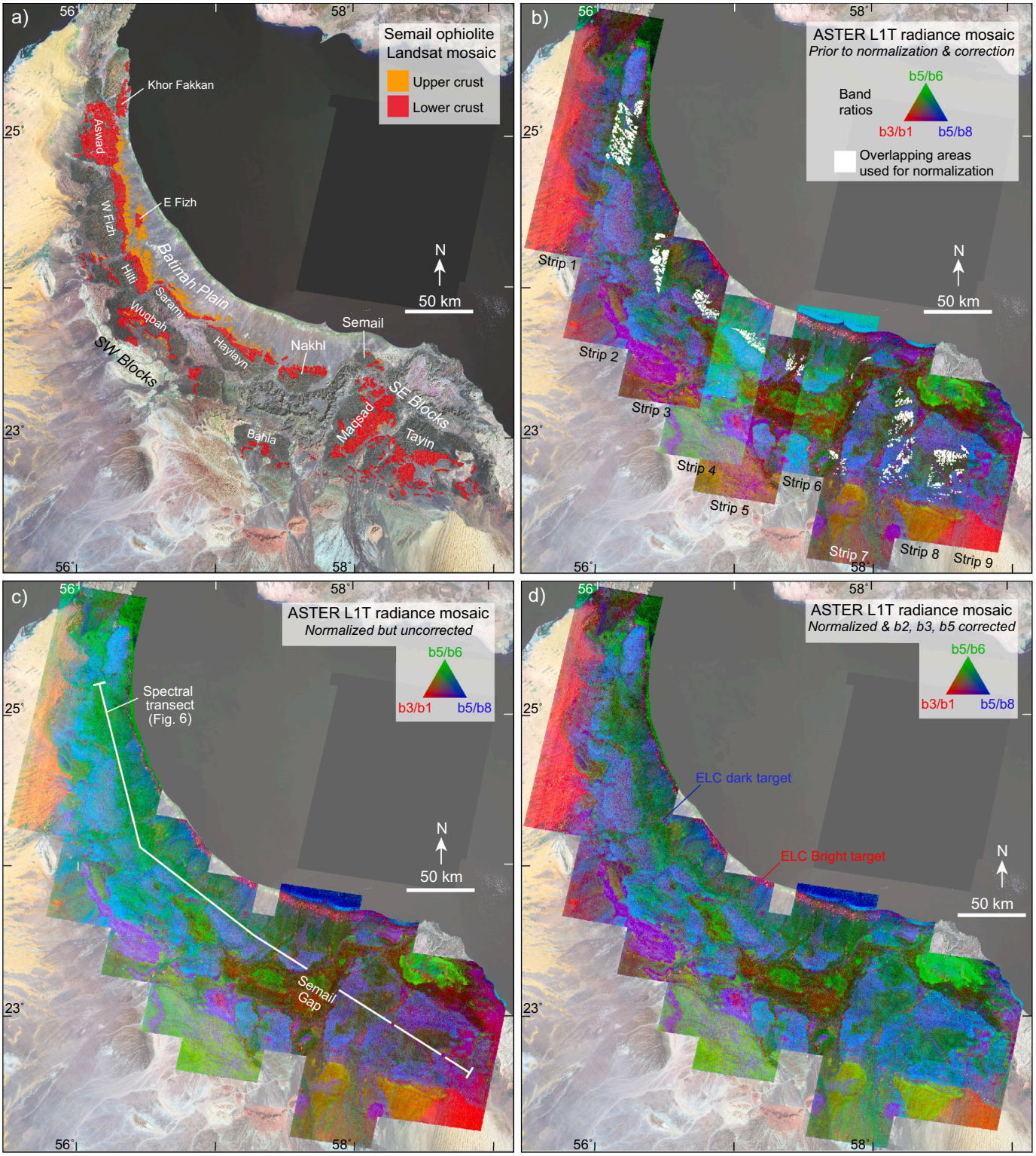

Fig. 5. Normalization and correction of the ASTER L1T radiance mosaic (Landsat TM background). a) Target ophiolite crustal outcrops, expanded from Belgrano et al. (2019). b) Radiance mosaic prior to normalization or correction. White polygons show overlapping areas using to calculate normalization statistics. c) Radiance mosaic following normalization but exhibiting b5/b6 fade and b3/b1 increase from W to E. d) Mosaic following normalization and correction of b1, b2, and b5 ramp errors.

cropping out along the Batinah Plain (Figs. 7b,d). These outcrops appear invariant between high-resolution imagery acquired in April 2009 and sampling in January 2018, supporting the similarity of our samples with the surface captured by ASTER in August 2007. Pixels from particularly flat and spectrally homogeneous areas of the limestone blocks were used to extract a mean L1T spectrum (Fig. 7c), and the outcrops were confirmed in the field as monotonous limestone completely free of vegetation (Fig. 7b). For both ELC targets, we took several samples and averaged repeat measurements on their originally upwards facing surfaces with the ASD Fieldspec3 contact probe (Fig. 7d).

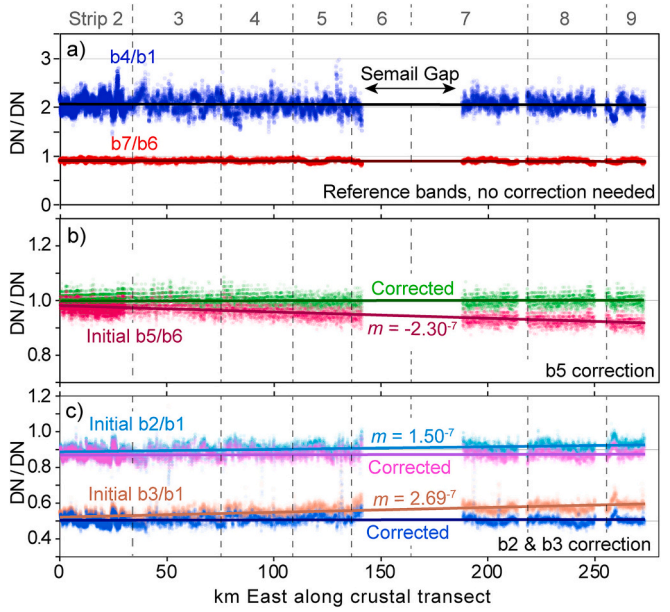

Fig. 6. Across-mosaic ASTER L1T band ratio transects and linear regressions showing ramp errors in data number (DN) ratios (m = slope) before and after correction. Dashed lines show mosaic strip boundaries. Transect location is shown in Fig. 5c. a) Well-calibrated reference bands 6 and 1. b) Linear decrease in b5 relative to well-calibrated b6 and linear regression following ramp correction with constant b5/b6 ratio, after Cudahy et al. (2020). c) Ramp errors for b2 and b3 relative to b1, regressed before and after correction.

Following ELC, some particularly dark pixels in the L1T radiance mosaic were initially calibrated to negative reflectance values. Over the targeted ophiolite crust, negative values made up 1–6% of the calibrated b1, b7, b8, and b9 pixels and < 0.5% of the other bands. The reasons for this are uncertain but could be related to dust on the sheeting in 2007, but not on the measured sample, or to local atmospheric scattering elevating the apparent reflectance of the dark target. To preserve this significant area of darker pixels for interpretation, an overall adjustment was made to the mosaic following ELC. The lowest calibrated value of any band within the target outcrop area was −0.1247, so 0.1247 was uniformly added to all bands over the entire mosaic. This uniform positive offset improves the coverage of our maps and does not affect spectral shapes, but it does slightly affect the absolute values of band ratios. Hence, any classification thresholds for band ratios would need to be redefined following the approach in Section 5.2 before reapplication to mosaics in other studies. Hereafter we refer to the corrected and offset ASTER mosaic as the Semail Reflectance Mosaic (SRM).

5. Spectral results and generation of alteration map

5.1. Field mapping of reference sites

Classification of the SRM was based on image data extracted from training or reference areas of field-mapped hydrothermal alteration. Some of these areas had already been mapped or described, such as the Ajeeb epidosite (Gilgen et al., 2016), the Salahi and Salahi-S chloritites (Miyashita and Adachi, 2020), and ultramafic intrusions with abundant serpentine (BRGM, 1993). We visited these sites to confirm what was reported and mapped and visited many new alteration zones (Table A1, Belgrano et al., 2022). The largest of these field maps and some of the reference pixels are shown alongside the remotely sensed map results in Section 6. A summary of our field mapping as well as Shapefile polygons of the reference pixels are available in the data archive (Belgrano et al., 2022).

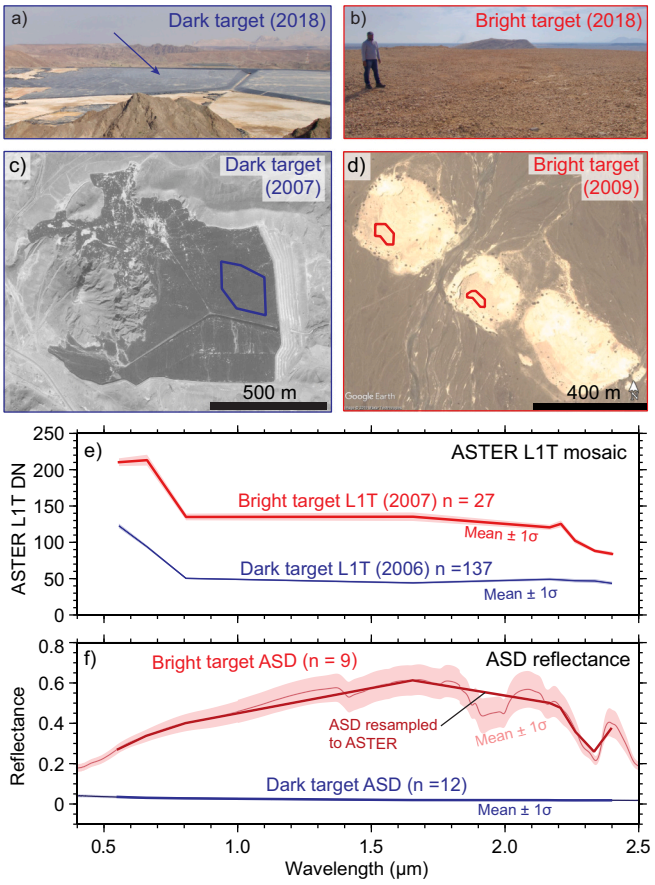

Fig. 7. Empirical line calibration (ELC) targets and spectra. a) Dark target: black plastic sheeting (2018). b) Bright target: limestone outcrops (2018). c) Dark target: OrbView-3 panchromatic image (Jan. 2007), showing sheeting condition close to ASTER acquisition. d) Bright target: Google Earth Image (April 2009). e) Normalized ASTER L1T mosaic mean ± 1σ, data number (DN) units. d) ASD Fieldspec3 mean ± 1σ reflectance measurements of the ELC target samples, also resampled to ASTER band passes. Target spectra are provided (Belgrano et al., 2022).

5.2. Alteration classification

To classify the SRM we used logical operator algorithms (LOA) implemented with the ENVI™ band math tool, adapting the approach of Mars and Rowan (2006) to mapping alteration in mafic crust (Table 1). Logical operator algorithms are a discriminatory classification tool, made up of a series of conditional statements regarding band reflectance values and ratios, such that pixels which satisfy all statements are positively classified initially as byte images. These classifications were additionally subdivided into degrees of alteration intensity (Section 5.3).

The necessary LOA statements and thresholds for discriminating each alteration type were defined using the statistical distributions of band reflectance values and ratios extracted from pixels over the field-mapped reference sites (Table A3, Belgrano et al., 2022). For the regional alteration, statistics were extracted from the entire field-mapped area at several different sites to capture the spectral variability of this extensive alteration type. For the localized alteration types, SRM statistics were selectively extracted from areas of pixels with the deepest b8 absorptions within areas of field-mapped intense hydrothermal alteration, to obtain reference spectra as close to endmember alteration intensities as possible. Features of the SRM reference spectra that are also present in the laboratory and library spectra were considered most characteristic and underpin each classification.

Table 1
Logical operator algorithms and spectral indices applied to the Semail Reflectance Mosaic and used to map hydrothermal alteration and other rock types. Adapted from the approach of Mars and Rowan (2006) for the target rock types and local reference data.

Classification or Index	Spectral Index/Logical operator algorithm (LOA)	Intensity multiplier
NDVI*	((b3 - b2)/(b3 + b2))	–
Fe-index	((b4 / b1) * (b3 / b1))	–
Non-vegetated outcrop†	(NDVI le 0.08) * (outcrop_area eq 1)	–
Map classifications		
Regional spilite and lower crustal alteration (Sect. 5.2.1–2)	((b5 / b8) le 1.36) * ((b6 / b8) le 1.35) * ((b3 / b1) ge 0.9) * (Fe-index le 2.8)	(b5/b8)
Epidosite alteration (Sect. 5.2.3)	((b5 / b8) ge 1.36) * ((b6 / b8) ge 1.28) * ((b5 / b4) ge 1.03) * ((b4 / b3) ge 1.27) * ((b9 / b8) ge 1.05) * ((b1 / b2) le 1.02)	(b5/b4)
Chlorite–epidote alteration (Sect. 5.2.4)	((b5 / b8) ge 1.36) * ((b6 / b8) ge 1.27) * ((b5 / b4) ge 0.98 and le 1.03) * ((b4 / b3) ge 1.22) * ((b1 / b2) ge 0.9 and le 1) * ((b5 / b3) ge 1.08) * ((b7 / b8) le 1.35) * ((b9 / b8) le 1.05)	(b5/b8)
Actinolite alteration (Sect. 5.2.5)	((b5 / b8) ge 1.36) * ((b6 / b8) ge 1.27) * ((b5 / b4) le 1.02) * ((b4 / b3) ge 1.27) * ((b9 / b8) le 1.1) * ((b1 / b2) ge 1.0)	(b5/b8)
Undifferentiated localized alteration (Sect. 5.2.9)	((b5 / b8) ge 1.36) * ((b6 / b8) ge 1.3) * (b4/b3 ge 1.2) * (Fe-index le 2.8)	(b5/b8)
Serpentinized ultramafic (Sect. 5.2.7)	((b5 / b8) ge 1.4) * ((b6 / b8) ge 1.26) * ((b5 / b4) le 0.93) * ((b4 / b3) le 1.3) * ((b5 / b3) le 1.09) * ((b1/ b2) le 0.93) * ((b7 / b8) ge 1.09) * ((b9 / b8) le 1.04) * (b9 le 1.7)	(b5/b8)
Umbers and Fe-rich rocks	(b1 /b2 le 0.91) * (b8 / b7 lt 1.03) * (Fe-index ge 2.8) * (b5 / b3 ge 1.4) * (b5 / b8 le 1.25)	(b5/b3)

*NDVI = Normalized difference vegetation index; †Appended to all LOAs, 'outcrop_area' is a binary image of the digitized crustal outcrop outline map, with crustal outcrop assigned a value of 1; eq = equals, le = less than or equal to, ge = greater than or equal to.

To discriminate hydrothermally altered rocks from anomalously Fe-rich lithologies such as gossans or metalliferous sediments (umbers), an Fe-index was constructed based on the strong absorption at b1 (0.5–0.6 μm) relative to b3 and b4 for these rock types in our reference areas (Table 1). Multiplication of the related b1/b3 and b1/b4 ratios improved the statistical separation between moderately Fe-rich andesites and extremely Fe-rich gossans and umbers. Absorption at 0.5 μm has previously been used to map Fe-oxide rich lithologies (Rowan and Mars, 2003), and is supported by the library spectra for hematite and goethite (Fig. 8a). The Fe-index also permitted umbers and similarly Fe-rich rocks to be classified (Table 1).

A maximum threshold for the normalized difference vegetation index of 0.08 (NDVI; Kalinowski et al., 2004), and a binary statement for the ophiolite crustal outcrop map expanded from Belgrano et al. (2019) were added to each LOA. This NDVI threshold is intermediate between the maximum NDVI of 0.065 for the regional alteration reference areas and the mean − 1σ of 0.09 for reference pixels of wadi vegetation. Together, these statements exclude the ophiolite mantle, large wadis and gravel terraces, and vegetation, restricting all classifications to areas of unvegetated ophiolite crustal outcrop, as well as any smaller gravel areas not delineated by the ~1:50 k scale outcrop map. This crustal outcrop map is provided in the data archive (Belgrano et al., 2022).

The utilized LOAs are listed in Table 1, and the key aspects of their construction are summarised for each alteration type below. The threshold values are specifically tuned to our ELC as well as to the overall positive offset we applied. The general LOA structures should be applicable to other case studies, but the specific threshold values would need to be revised based on local reference data.

5.2.1. *Regional spilite alteration of the upper crust*

Resampled to ASTER band passes, the SRM reference spectra for regional alteration in the different upper-crustal units are closely comparable with one another (Fig. 8c). For this reason, we grouped and averaged all of the field-mapped areas of upper crustal spilite alteration into a single, undifferentiated reference spectrum for this alteration type (Figs. 8b and c).

Weak absorption at ~2.3 μm and a resulting low b5/b8 reflectance ratio most sensitively discriminates regional alteration from the other localized alteration types. This difference is well explained by the relatively flat spectra of the constituent anhydrous silicate minerals clinopyroxene, albite, and quartz mixed with minor chlorite, as well as by the hand sample spectra, and therefore it is considered reliable (Fig. 8a). As some of the minor minerals in the regional alteration also define the localized alteration types, the difference between regional and localized alteration is mineralogically and spectrally transitional. A universal threshold between regional and localized alteration was determined statistically at the b5/b8 mean + 2σ upper limit of the regional alteration reference pixels. Additional thresholds to exclude iron-rich umbers and gossans were applied to b1/b3 and b3/b4 at the reference data minima and maxima, and to b6/b8 to exclude any altered rocks with noisy or crosstalk-affected b5.

Despite being weaker than that of the localized alteration types, the SRM reference spectrum for regional alteration does show absorption at 2.30–2.36 μm (b8), consistent with either minor chlorite, actinolite, epidote, prehnite, serpentine, or carbonate, which are all common minor constituents of the regional alteration at different crustal levels (Sect. 1.2–1.3). This suggests that variations in the abundance of these undifferentiated minerals within the regional classification can be mapped by absorption in b8.

5.2.2. *Regional lower crustal alteration*

As the regional alteration classification was designed to encompass the diversity of upper crustal volcanic and intrusive rocks, including gabbros, it was also applicable to the lower crust. Despite their textural differences, the lower and upper crust have related primary and secondary alteration mineralogy (Stakes and Taylor, 1992). For both basaltic and gabbroic protoliths, alteration by any of the common OH-bearing minerals produces absorption at ~2.3 μm, increasing b5/b8 from a fresh value near unity (Fig. 8a). This is supported by the similar spectrum of the regionally altered lower crustal gabbro and upper crustal lavas (Fig. 8b). The major advantage of classifying the upper and lower crust together is that alteration intensity can be mapped continuously across their boundary. However, we note that the regional alteration classification and lower intensity cut off is based on an upper-crustal reference. Hence, classification performance may be somewhat better for the upper crust.

5.2.3. *Epidosite*

The lab and SRM reflectance spectra of epidosites are dominated by the deep 2.34 μm absorption of epidote (Fig. 8). This feature, as well as the distinctly high b5/b4 and b9/b8 of the epidote library spectrum are reasonably-well reproduced in the epidosite hand sample and SRM reference spectra, and hence these features underpin the epidosite classification. A lower threshold for b5/b4 and b9/b8 discriminates epidosite from chlorite–epidote and actinolite alteration, and an upper b1/b2 threshold of 1.0 provides additional discrimination from actinolite.

5.2.4. *Chloritite and chlorite–epidote alteration*

A complex LOA was constructed in an attempt to map chloritite

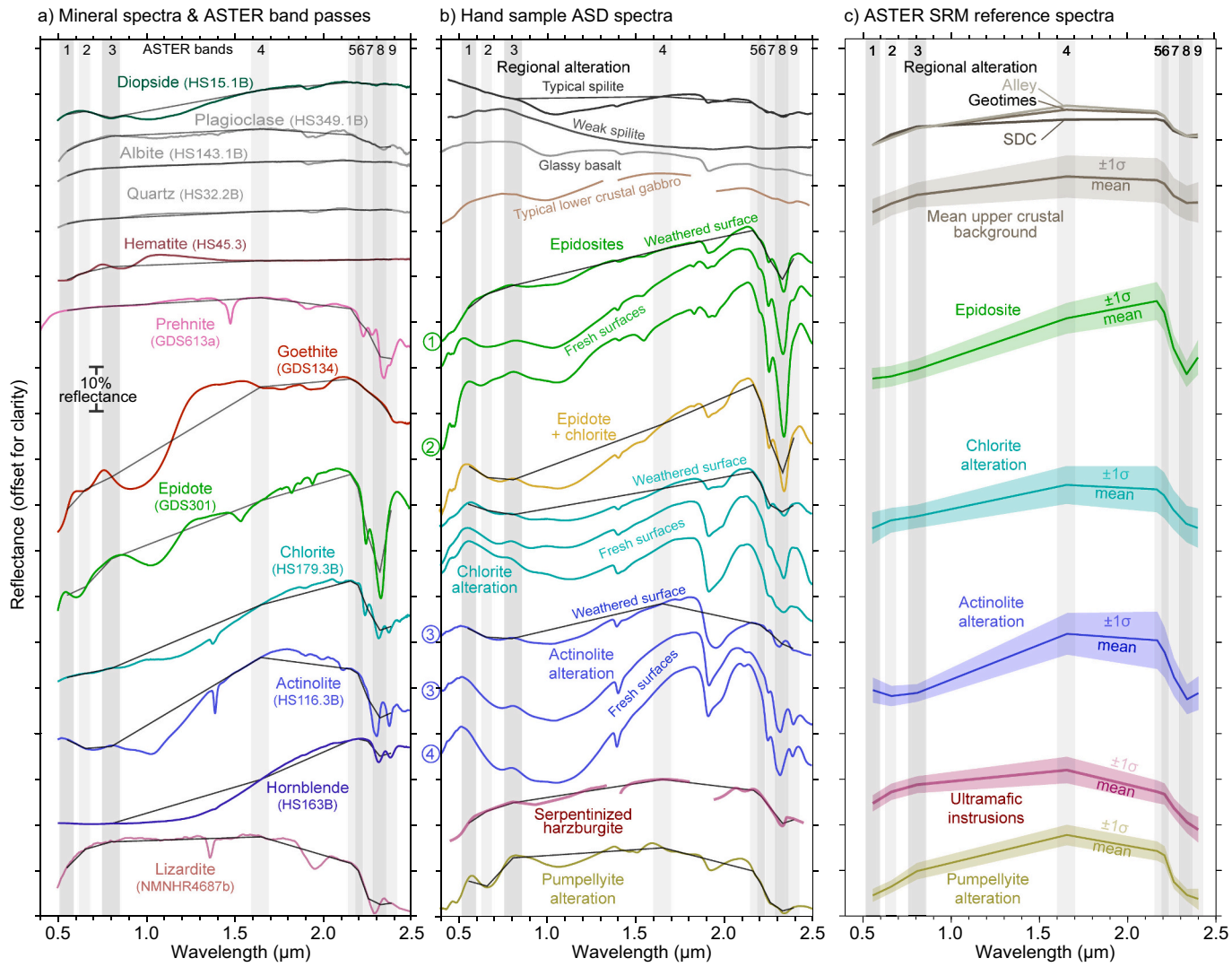

Fig. 8. ASTER band passes and reflectance spectra of the target alteration types and minerals. a) USGS Spectral Library (v7; Kokaly et al., 2017) spectra of the target minerals in the target alteration types. b) Reflectance spectra of rock samples of the target alteration types measured by ASD FieldSpec3, except the gabbro and harzburgite spectra (Roy et al., 2009). Black lines are resampled to ASTER band passes. Sample localities numbered 1–4 are marked in Figs. 10–11. c) Mean ± 1σ of reference spectra extracted from the Semail Reflectance Mosaic (SRM) over areas of field-mapped hydrothermal alteration.

alteration, taking advantage of b9/b8 and b5/b4 suppression by chlorite for discrimination from epidosite, and b1/b2 and b5/b4 thresholds to discriminate from actinolite. Despite this, extremely low albedo and subtle spectral features meant we could not reliably discriminate chloritite alteration. Upon assessment of the anomalies mapped by the chlorite-optimized LOA, we found that this classification instead reliably delineates areas where both chlorite and epidote are present (see Sect. 6.3.2). Chloritite classification should be more possible with hyperspectral imagery (e.g., Dalton et al., 2004; Sivitskis et al., 2018).

5.2.5. *Actinolite alteration*

The actinolite library spectrum is well reproduced by both the hand sample spectrum and the SRM actinolite reference spectrum, even after resampling to ASTER band passes (Fig. 8). These features, particularly high b1/b2, b4/b3, b5/b8 and low b5/b4 and b9/b8, were readily used to discriminate actinolite alteration.

5.2.6. *Pumpellyite alteration*

Our lab measurements of Fe^{3+}-pumpellyosites reproduce the characteristic pumpellyite absorption triplet near 1.5 μm and the absorption at ~2.34 μm with a low shoulder at 2.4 μm (White et al., 2017). The general features of the pumpellyosite lab spectrum are well-reproduced by the SRM spectra. However, several key band ratios overlap with the regional alteration, and we were therefore unable to construct a reliable pumpellyosite classification. Some areas classified as regional or undifferentiated localized alteration will therefore contain unrecognized pumpellyosite. It may prove possible to map pumpellyosite alteration with hyperspectral imagery, to which end the reference areas and spectra have been provided (Fig. S2 and Belgrano et al., 2022).

5.2.7. *Serpentinized ultramafics*

The library spectrum of lizardite, a common serpentine mineral in Oman (Nehlig and Juteau, 1988), with its deep 2.3 μm (b8) absorption and relatively high b4/b5 ratio, is well reproduced by the partially serpentinized harzburgite spectrum as well as the ultramafic intrusion SRM reference spectrum (Fig. 8). This high b4/b5 ratio, as well as low b1/b2, b8/b9, and b5/b3 thresholds were used to discriminate serpentinized ultramafic rocks throughout the crust.

5.2.8. *Undifferentiated localized alteration*

To reduce false positives related to spectral noise and variability, numerous logical operator terms were employed, often resulting in

spatially patchy localized classifications. To help interpret across these patchy classifications as well as the gradational peripheries of alteration zones, we also generated a classification for 'Undifferentiated localized alteration' for rocks with 2.33 μm (b5/b8) absorption above that of the regional background that could not be differentiated further. This encompasses epidote, chlorite, and actinolite alteration and any mixture thereof.

For the crustal outcrops along the NE side of the ophiolite and in the SE blocks, this undifferentiated class is clipped by the set of more exactly differentiated localized alteration classes. On the SW side of the ophiolite, where residual normalization errors across the mountains prevented accurate discrimination of the spectrally similar alteration types, only this undifferentiated localized alteration and the regional alteration classes are mapped.

5.3. Alteration intensity multipliers

To facilitate interpretation of the spatial zonation of alteration intensity, we multiplied each pixel of each class by an 'intensity multiplier'. These multipliers are reflectance band ratios which, based on the reference and library mineral spectra, are sensitive to the amount of the key alteration minerals in each classified pixel. A b5/b8 multiplier maps the intensity of undifferentiated alteration minerals within the regional spilite and lower crustal alteration. A b5/b8 multiplier was also used for the localized chlorite–epidote, actinolite, and serpentinized ultramafic alteration types. For epidosite, b5/b4 was used as an intensity multiplier instead, as this ratio is characteristically high for epidosite but less so for the other SRM reference spectra (Fig. 8).

The continuous ranges given by the multiplier for each classification were then split into ten intervals between the lower cut-off for that classification and the mean + 2σ upper value of each endmember reference pixel distribution. This range maps the intensity of alteration in a useful but only semi-quantitative way, as it does not account for potential mineral mixtures or non-linear spectral mixing.

6. Alteration map results and validation

The utility of the alteration map produced by this study depends on its positional, spectral, and most importantly, geological accuracy, which are assessed in the following.

6.1. Positional accuracy

ASTER L1T scenes are terrane-corrected using an elevation model with a positional accuracy of 25 m or better, but the absolute positional accuracy of the corrected imagery is influenced by topography (Meyer et al., 2015). Relative to four reference points that we defined at road intersections and outcrops by handheld GPS (± 5 m), we recorded positional errors in the ASTER L1T VNIR imagery of 10–22 m, with a root mean square error (RMSE) of 16 m. This error is within the uncertainty with which the reference points could be defined in the image. Qualitative comparison with our GPS-guided field maps further indicates that ASTER L1T positional errors are generally less than two 15 m pixels, as are the positional mismatches between ASTER L1T strips. The positional accuracy of ASTER L1T over the crustal outcrop areas is therefore sufficient for direct comparison of ASTER and field maps.

6.2. Spectral accuracy

As the SRM was classified using image-derived data, the absolute spectral accuracy of the mosaic is of secondary importance to the geological accuracy of the final map. Nevertheless, a spectrally accurate mosaic facilitates comparison with sample spectra and supports the effectiveness of our processing. A spectral check was performed by qualitatively comparing the SRM reference spectra with sample and library spectra for each alteration type (Fig. 8).

The overall shapes of the sample spectra are relatively well-reproduced by the SRM, including the key b1/b2, b4/b5, b5/b8, and even b9/b8 ratios that underpin the classifications. This suggests that our pre-processing has alleviated some of the persistent issues with ASTER b5, b8, and b9 (Hewson et al., 2005; Mars and Rowan, 2010). The greatest discrepancy is the elevated VNIR reflectance of chlorite alteration in our laboratory spectra, which also affects the spilites (Fig. 8b). This could be due to Fe-oxide rinds on the outcrop surface but not on the laboratory samples, supporting our approach of basing classification on image-derived reference data.

6.3. Geological accuracy and utility

The success with which our ASTER classifications can predict the mineralogy, geometry, and intensity of hydrothermal alteration is the most important criterion of accuracy for the final map and the workflow that generated it. The assessments below test this accuracy and hence establish the geological utility of the final alteration map.

6.3.1. Field mapping comparisons

For alteration types that are readily recognizable in the field, such as epidosite, chloritite, and serpentinised ultramafics, geological accuracy was primarily assessed by comparing the ASTER classified areas with field-mapped sites (Figs. 9–11). The classifications are presented clipped to the field maps for direct 'ASTER comparison', and also in their full 'ASTER Alteration Map' version, demonstrating its superior coverage. In addition to the illustrated sites, many others were visited and the ASTER predictions verified as correct for the majority of cases. All major sites and descriptions of their classification performance are listed in Table A1 (Belgrano et al., 2022).

Reference pixels used to build the LOAs were partly selected from several of these reference sites: Hilti N, Ajeeb, Rusays, Lasail S (Figs. 9a, 10a–b, 11a). These examples are hence somewhat circular comparisons; nevertheless, they demonstrate the performance of the classifications near the reference pixels. Reference pixels were not extracted from the other sites: Safwa, Duqal, Rajmi N, and Salahi N (Figs. 9b, 10c, 11b, c), hence these comparisons serve as independent cases for geological validation of the alteration map.

To assess whether some areas of localized alteration might have been missed by our classifications (false negatives), we also field-mapped in an area where only regional alteration was predicted by the ASTER SRM map (Safwa, Fig. 10b). Typical regional spilite alteration does dominate the field map, but some small areas of localized epidosite and chlorite alteration are also present. Within these areas, localized alteration is patchy, making up less than a few tens of area% of the outcrops at the pixel scale, which was not detectable by ASTER. This assessment demonstrates that our remotely sensed map is only capable of delineating alteration zones that are relatively continuous over at least 30 × 30 m. Patches of alteration smaller than this, which are common for all localized alteration types, are accordingly not shown by our map. The remotely sensed areas therefore represent *minimum* possible areas for the localized alteration types and *maximum* possible areas for the regional alteration.

For epidosites, the accuracy of the ASTER map is supported by the reproduction of epidosite zone geometries and intensities around Wadi Hatta (Fig. 10a) and at Rusays and Shiyya (Fig. 10b). No reference pixels were extracted from the Duqal epidosite, and it is situated in ASTER Strip 4, two strips away from the epidosite reference pixels in Strip 2. The accurate prediction of this epidosite's geometry and moderate intensity in a different part of the mosaic than the reference data strongly supports the predictive geological accuracy of our map and the steps that generated it (Fig. 10c).

For actinolite, the ASTER map correctly predicted the presence of intense actinolite alteration that was field-mapped and sampled in Lasail and Boninitic Alley lavas in the E. Fizh and Hilti blocks (Figs. 9b, 10b, 11). Actinolite alteration can be subtle or even cryptic in the field,

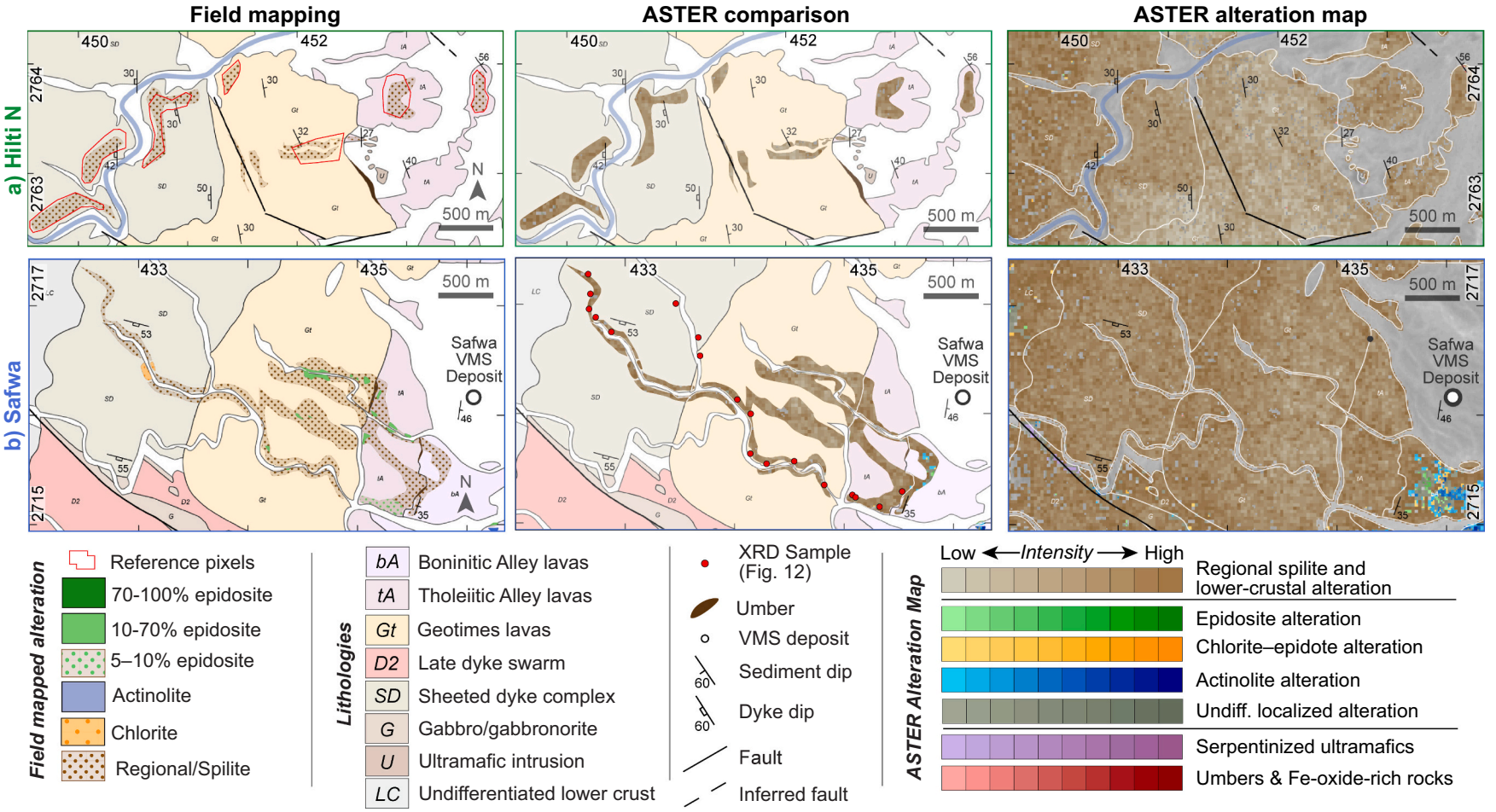

Fig. 9. Field-mapped regional spilite alteration versus ASTER SRM classifications. Left: field-mapped alteration; Middle: ASTER alteration maps clipped to the field-mapped areas for direct comparison; Right: complete ASTER alteration maps over b1 greyscale images. Geological base maps from Belgrano et al. (2019). Reference pixels are outlined in red. a) Hilti North, discontinuous mapping (due to access) of regional spilite alteration. b) Safwa upper-crustal control site field-mapped over an area where ASTER predicts no localized alteration types, showing XRD sample locations. Grids are WGS84/UTM 40N.(For interpretation of the references to colour in this figure legend, the reader is referred to the web version of this article.)

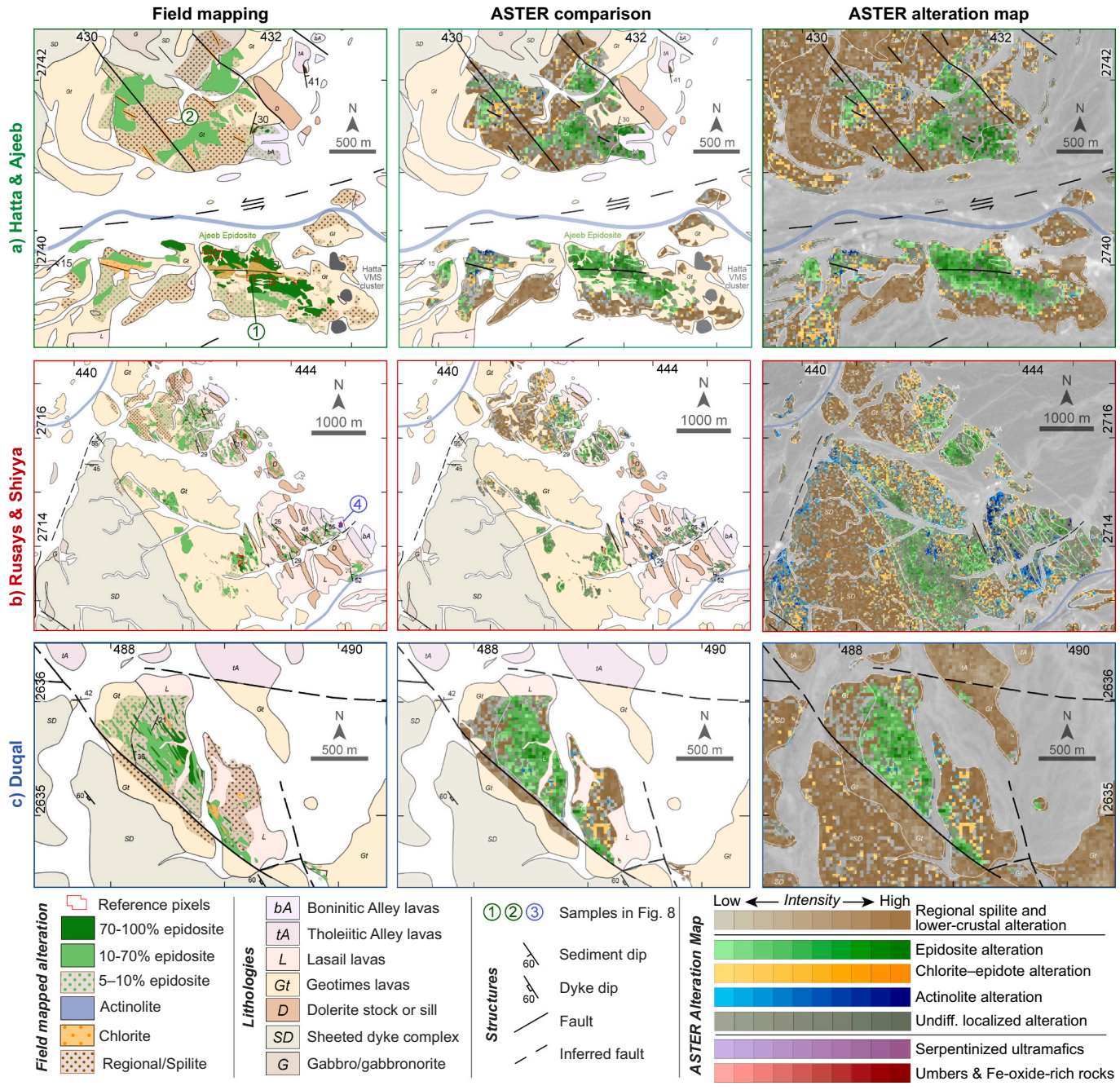

Fig. 10. Field-mapped epidosites versus ASTER SRM classification. (a) Ajeeb epidosite field map after Gilgen et al. (2016), Hatta Zone/Fizh block. (b) Rusays and Shiyya epidosites, E. Fizh block, field-mapped sub-areas and swathes. (c) Duqal epidosite, Sarami block, independent validation site not used for reference spectra. Grids are WGS84/UTM 40N.

however, so this assessment is expanded in Section 6.3.2.

The chlorite–epidote classification correctly predicts locally intense chlorite and epidote alteration in the SDC at the Rajmi N site (Fig. 11b) and small areas of chloritized epidosite in the Duqal epidosite (Fig. 10c). This classification did not differentiate the central area of chloritite overprinting epidosites at Ajeeb, probably due to the abundance of relict epidote there. Areas of intense black chloritite such as at Salahi N and elsewhere in the Fizh and Hilti blocks (Miyashita and Adachi, 2020) do not produce a characteristic ASTER response, and are hence mostly undifferentiated in our map (Fig. 11c; also Sect. 5.2.4).

The serpentinized ultramafic classification reliably delineates ultramafic intrusions in the crust as uniformly dark purple zones in our map. Mixed peridotite/gabbro intrusions and layered gabbros in the crust–mantle transition zone typically appear as patchy purple zones (e.g., Fig. 11c). The Umber and Fe-oxide-rich classification also successfully detects the numerous large outcrops of umbers mapped by BME (1987) in the Hilti block, as well as the corridor of small Fe-oxide-rich gossans in the 'Bowling Alley' between Wadis Fizh and Jizi (Belgrano et al., 2019). However, many umber outcrops are too small to be detected by ASTER, and some of the larger gossans such as Zuha are not well mapped, potentially because their upper surfaces consist mostly of residual silica.

An important consideration for using the map is that the true areas of exposed bedrock are less extensive than suggested by the ~1:50 k scale outcrop outlines used to clip the classifications (Figs. 9–11). This means that some areas of colluvial gravel between outcrops are unavoidably

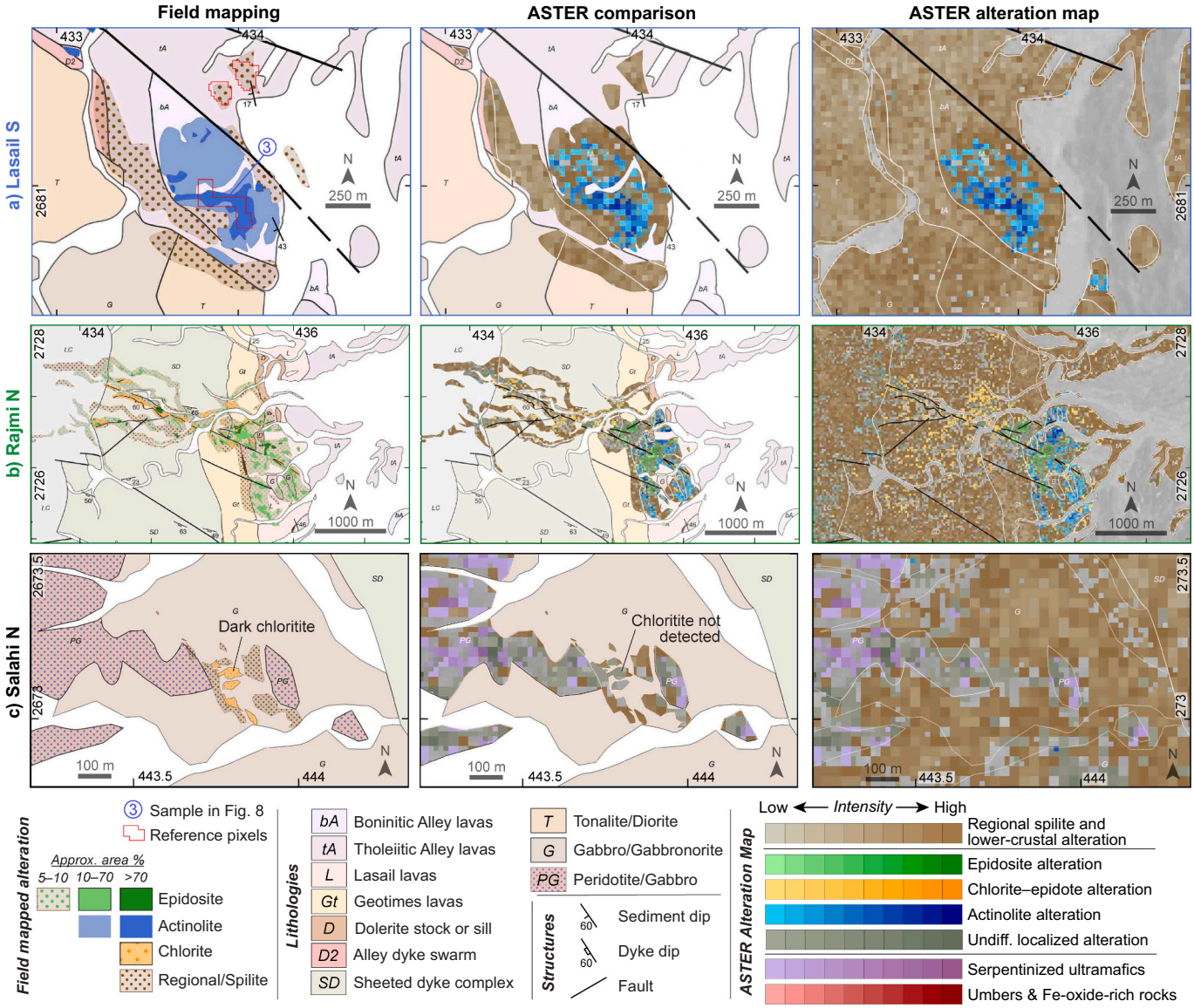

Fig. 11. Field-mapped actinolite and mixed alteration sites versus ASTER alteration classifications (variable scales). a) Lasail South actinolite alteration. b) Rajmi North, *E*-dipping upper crustal section with mixed chlorite and epidosite alteration in the sheeted dyke complex, and epidosite and actinolite alteration in the overlying Geotimes and Lasail lavas. c) Salahi N chloritite in lower crustal gabbro reported by Miyashita and Adachi (2020), undifferentiated by our map. Peridotite/gabbro area adapted from BME (1987). Grids are WGS84/UTM 40N.

included in the alteration map. Outside of large wadis, however, these gravels spectrally reflect the mineralogy of the nearby bedrock outcrops (Fig. 9–11), and hence still provide useful information on the presence and extent of alteration zones.

6.3.2. *ASTER anomaly sampling and XRD mineralogy*

In the field, it is often challenging to discriminate localized actinolite or chlorite–epidote alteration from regional spilite alteration, including at several ASTER anomalies we visited for map validation. For example, large areas of actinolite alteration at Rajmi N were missed during mapping (Fig. 11b). To assess the performance of these ASTER classifications, we.

collected 27 samples from actinolite ASTER anomalies and 14 from chlorite–epidote anomalies for quantitative XRD mineralogy. The samples were selected at random, based only on their location within classified pixels, not on their particularly altered appearance. The analysed mineral contents are plotted with those of 53 samples collected along upper crustal transects at Safwa and Salahi classified by ASTER as regional alteration (Fig. 9b), which serve both as a baseline for comparison and to mineralogically validate the regional alteration classification (Fig. 12a, b).

Among samples from the ASTER actinolite anomalies, 25/27 (93%) have >5 wt% actinolite. This contrasts with 44/53 (83%) of the ASTER regional spilite samples containing <5 wt% actinolite (Fig. 12a). Only two actinolite anomaly samples contain no actinolite, both from Lasail lavas, and instead contain slightly elevated (9 and 23 wt%) prehnite. This could be due to the gap in representativeness between hand sample and pixel but could possibly also be a false positive that users should be aware of. Overall, Fig. 12a demonstrates that the regional and actinolite classifications correctly discriminate between actinolite-poor and actinolite-rich rocks respectively in at least 80–90% of cases and suggests that the lower threshold for discrimination is around 20 wt% actinolite.

Samples from ASTER chlorite–epidote anomalies contain moderate amounts of chlorite and epidote, with epidote being generally elevated above the regional background (Fig. 12b). Combined with the field

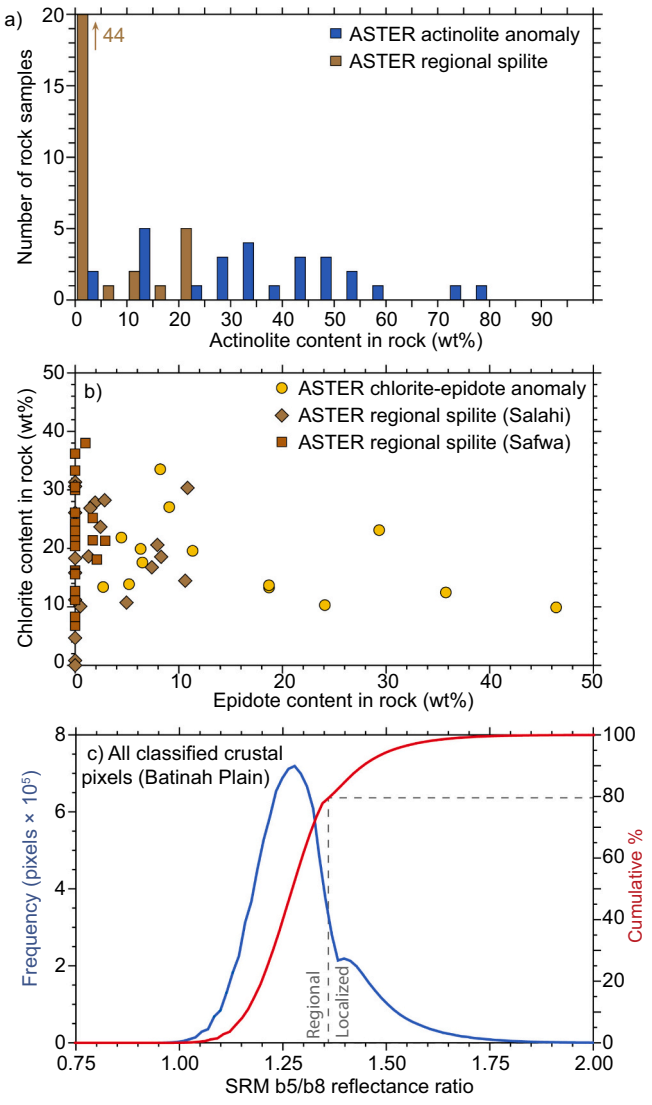

Fig. 12. Mineralogical assessments and alteration intensity of the ASTER alteration map. a) Histogram of actinolite content in samples from ASTER actinolite anomalies vs. ASTER regional spilite pixels. Bins = 5 wt%. b) Chlorite vs. epidote contents for samples collected from ASTER chlorite–epidote anomalies and ASTER regional spilite alteration. Chlorite is the sum of pure chlorite plus the fraction of chlorite in interlayered chlorite–smectite. c) Frequency and cumulative distributions of b5/b8 reflectance ratios. Bin = 0.015 and frequency smoothed with a three-bin moving average. The b5/b8 upper threshold for the regional alteration classification is dashed in grey (1.36).

comparison at the Rajmi N SDC (Fig. 11b), where areas of chlorite and epidosite alteration mixed at the outcrop scale are classified as chlorite–epidote alteration, Fig. 12b demonstrates that this classification delineates chlorite and epidote alteration mixed at any scale smaller than an ASTER pixel. In most cases, chlorite contents are not elevated above the regional background and the b5/b8 signal must predominantly originate from epidote. However, chlorite is consistently present to some extent, providing the b9/b8 and b5/b4 suppression that differentiates the chlorite–epidote and epidosite classes.

6.4. Map products and remote sensing toolkit

Fig. 13 shows part of the final alteration map generated by the methods described above. The full size and high resolution versions of the alteration map are provided in the Data Archive (Belgrano et al., 2022). Archive map sheets 1a and 2a contain the complete ASTER alteration map, equivalent to Fig. 13. Map sheets 1b and 2b show only the localized alteration classifications with the regional alteration excluded to reveal an underlying geological base map and resampled at a suitable resolution. This base map is adapted from the companion geological map in Belgrano et al. (2019) and expanded with ASTER imagery and maps from Goodenough et al. (2010) and Nicolas et al. (2000). As such, the base map has greater detail over the central ophiolite mapped in Belgrano et al. (2019).

These alteration maps are provided in the Archive as undecorated but native resolution georeferenced images, high-resolution but compressed maps decorated with grids and legends, and georeferenced vectors for GIS analysis but without intensity information (Folder A3; Belgrano et al., 2022). Alongside the final map products, we have archived a toolkit for remote sensing and sensor testing in the Semail ophiolite, with all the field and reference data required to reproduce this study or to reapply it with different targets or sensors (Folder A2; Belgrano et al., 2022).

7. Discussion

7.1. Areal proportions of the different alteration types

The classified areas for each alteration type for the entire mapping area, the Batinah Plain, and each ophiolite block are summarised in Table S5, and the relative abundances of the alteration types are reported in Table S6 as fractions of the total classified area, under the assumption that this approximates the area usefully surveyed by ASTER and normalizes for unclassified outcrop.

The Batinah Plain is a near continuous oblique exposure of oceanic crust and is hence a geologically interesting region to consider. Along the Plain, 83 area% of the crustal outcrop is classified. This includes 90 area% of the upper crustal outcropsand 79% of the lower crustal outcrop, confirming slightly better classification performance in the upper crust (see Sect. 5.2.2). Regional spilite and lower crustal alteration dominates the ophiolite crust (78 area%). Classified areas of localized alteration are much smaller, with epidosite, chlorite–epidote, and actinolite alteration making up only 0.34 area%, 0.63 area%, and 0.92 area% respectively along the Batinah Plain, but reaching up to 1.1 area %, 3.6 area%, and 6.0 area%, respectively, in the East Fizh block (Fig. 11b, Table S5). It is to be recalled that the area fractions of localized alteration are minimum estimates (Sect. 6.3.1).

The areal dominance of regional alteration is also apparent from the b5/b8 reflectance ratio distribution along the Batinah Plain (Fig. 12c). As a proxy for alteration intensity, the frequency distribution of the b5/b8 ratio attains a peak at ~1.28 and approaches zero at unity. The primary mineral and laboratory spectra of the fresh and weakly altered rocks show that unaltered mafic crust should have a b5/b8 ratio near unity (Fig. 8). That the b5/b8 frequency ascends from unity without having been forced to do so strongly supports the precision and accuracy of our ELC and the effectiveness of the intensity multiplier for mapping the intensity of regional alteration. The distribution further shows that such fresh rocks are exceedingly rare, and that relatively high background alteration intensities are the norm, as previously asserted by field and petrological studies (Alabaster and Pearce, 1985; Pflumio, 1991).

7.2. Remote sensing of spectrally similar alteration types

7.2.1. Base imagery and reflectance calibration strategies

For the base imagery, we found the precise terrane correction and geolocation of the ASTER L1T product more advantageous for mosaic normalization and comparison with field mapping than the reflectance correction of the ASTER 07XT level two reflectance product. However, this preference was influenced by the availability of ELC targets. Combining precision terrane correction *and* atmospheric correction using synchronously acquired atmospheric data (Mars and Rowan,

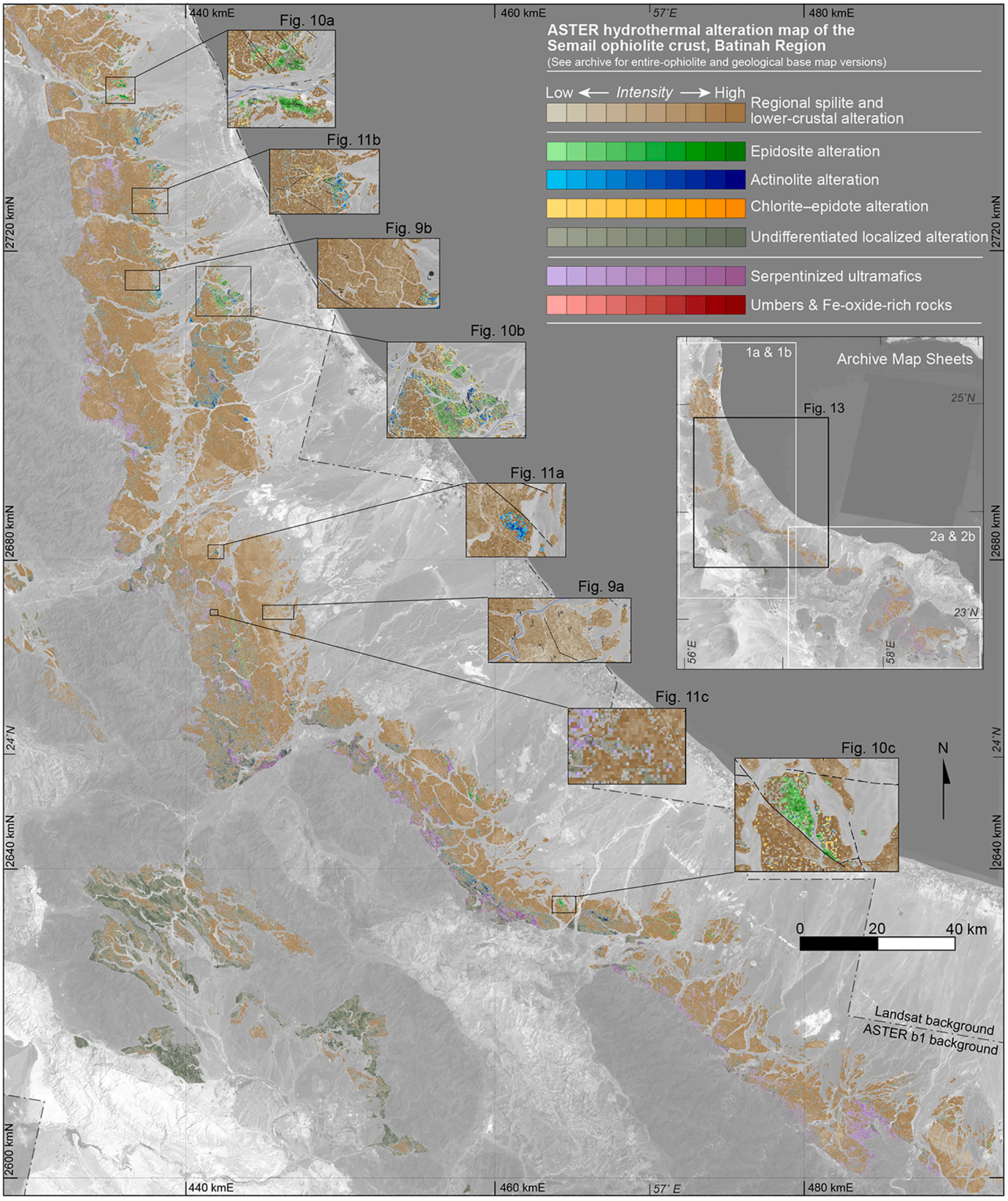

Fig. 13. Batinah Plain extract of final ASTER hydrothermal alteration map. The alteration classifications are clipped to the outlines of ophiolite crust, excluding the ophiolite mantle, and overlain on a greyscale b1 mosaic of the Semail Reflectance Mosaic (SRM; this study). For context, the ASTER b1 mosaic is overlain on a Landsat TM mosaic (1987) extending to the boundary. Grids are shown in both WGS84/UTM 40N (km) and WGS 84 (°Lat/Lon). Inset 'Archive Map Sheets' shows the extent of the full new ophiolite map sheets (Belgrano et al., 2022).

2010), together with correction of the systematic detector array miscalibration in b5 and possibly b2 and b3 (Fig. 6; Cudahy et al., 2020) would improve the regional mapping utility of ASTER reflectance products.

Ideally, more than two targets would have been used for ELC, and calibration spectra would have been collected in situ with a hyperspectral camera. Hyperspectral images of the targets would better take into account surface heterogeneity or shadowing, allowing additional targets to be used (e.g., gravel, sand). The limestone target also shares a similar spectral shape with the target alteration types, hence, any discrepancy between the surfaces measured by ASTER and by ASD Fieldspec3 could systematically interfere with the corrected SRM alteration spectra, which would be alleviated with additional targets.

In support of our approach and the utility of the archived target spectra for future ELCs, the corrected image spectra reproduce the laboratory measurements of the altered samples favourably (Fig. 8), and as mentioned above, the b5/b8 frequency distribution approaches zero at unity, as expected. Crucially, however, as our classifications are based on image data, any residual error in the reflectance correction is accounted for by tuning the LOAs. For the same reason, similar mapping results could be achieved using radiative transfer model calibration.

7.2.2. Optimized mosaic normalization

Initial attempts to spectrally normalize the ASTER mosaic using standard approaches yielded a mosaic that was insufficiently normalized for regional discrimination of spectrally similar alteration types. Our approach of firstly excluding scenes with residual atmospheric water features, and then selecting overlapping areas for normalization statistics exclusively from the target areas resulted in adequate normalization over these areas (Figs. 5, 6). Compared to previous approaches (e.g., Du et al., 2001; Hewson et al., 2005), this method trades normalization accuracy in the untargeted areas of the mosaic for improved accuracy in the targeted areas. However, our screening for residual atmospheric water features is relatively subjective. Further spectral investigation of such features through comparison of multi-temporal datasets may afford a more automated screening method.

Nevertheless, our highly case-study-optimized approach to mosaic generation allowed ASTER bands affected by crosstalk and atmospheric water vapor (b5, b8, and b9) to be employed in LOAs, which proved crucial for discriminating the spectrally similar alteration types. These steps may also improve mosaic normalization in other remote sensing applications and platforms, in particular for new narrow-swath hyperspectral data requiring many scenes to cover an area, such as PRIMSA, EnMap, HISUI, or EMIT.

7.2.3. Across-mosaic ASTER ramp errors

Across-scene ASTER b5 miscalibration issues over China (Cudahy et al., 2020) are also present in data collected over the Arabian Peninsula from 2000 to 2007 (Fig. 5c, 6). Resulting ramp errors need to be corrected when normalizing multi-temporal ASTER imagery by overlapping-edge statistics. Apparently comparable across-mosaic ramp errors are present in ASTER b2 and b3. Similar miscalibration is a possible explanation, but errors introduced by bi-directional reflectance distributions from the moderate relief terrane could also be considered (e.g., Li et al., 2012).

Regardless of their origin, spectral transect assessments and mosaic-wide corrections sufficiently eliminate these ramp errors for regional mapping of spectrally similar rock types (Fig. 6). Failing to make these corrections results in systematic across-mosaic errors in classifications employing ASTER b5, b2, and b3 (e.g., NDVI), precluding the discrimination of spectrally similar rock types and obscuring the true potential of the imagery.

7.2.4. Classifying spectrally similar hydrothermal minerals with ASTER

Epidote, chlorite, actinolite, and serpentine are common alteration minerals with spectral similarities, especially in multispectral data, but differing geological significance in mafic VMS systems. They have necessarily been lumped together in past ASTER classifications (Kalinowski et al., 2004; Mars and Rowan, 2010), and are challenging to discriminate even with hyperspectral data (Dalton et al., 2004). This may have limited the uptake of ASTER remote sensing of hydrothermal alteration in ophiolite and greenstone belt VMS districts. In this study, we reliably differentiated epidosite, actinolite, and serpentinite alteration from the regional background alteration in mafic crust. For pure chloritite alteration, low albedo and subtler spectral features prevented reliable detection and discrimination with ASTER. Mixed chlorite–epidote alteration was, however, reliably discriminated from the other alteration types by the combination of deep b8 (2.33 μm) epidote and chlorite absorption and b5 and b9 suppression by chlorite.

Production of a target-optimized, normalized reflectance mosaic and classifications based on image-derived reference data proved instrumental in discriminating the spectrally similar alteration types. Definition and use of image reference areas requires field work, but essentially eliminates the dependence of classifications on atmospheric correction accuracy and intrinsically accounts for local surface conditions.

In comparison to more sophisticated methods, the LOA classification approach is simplistic but also transparent in its operation (Mars and Rowan, 2006). These qualities allow for the straightforward integration of spectral and contextual knowledge. As in Mars and Rowan (2006), just a few key terms serve a central discriminatory role in each of our classifications (e.g., b5/b8, b5/b4, b1/b2 thresholds). However, the addition of several more loosely defined terms helped to reduce false positives. While this worked well for the near contiguous outcrops targeted along the Batinah Plain and even into the Southeastern blocks, our LOAs were so case-specific that they could not reliably discriminate epidosite on the SW, inland side of the Hajar mountains, where atmospheric conditions are somewhat different. Locally specific classifications are therefore demonstrably necessary to discriminate spectrally similar rock types with multispectral data. Emissivity spectra suggest that TIR discrimination of anhydrous silicates could powerfully complement the SWIR bands if a comparable level of spatial resolution were achieved (Fig. S2). However, at present, the alteration map performance produced using LOAs applied to the nine VNIR and SWIR bands is sufficient for many geological applications.

7.3. Crustal hydrothermal architecture

To our knowledge, our new map and its quantified areas represent the largest continuous spatial survey of hydrothermal alteration yet presented for oceanic crust. Full interpretation of this map is beyond the scope of this article. However, some initial observations can be made on crustal-scale hydrothermal architecture.

Our alteration maps (Figs. 10, 11) and areal comparisons (Table S6) confirm that localized epidosite and chlorite–epidote alteration are largely confined to the upper oceanic crust (Fig. 1b). The formation of epidosites requires reaction with vast quantities of modified seawater (water/rock mass ratios of ~700–40,000; Weber et al., 2021). The situation of epidosites thus suggests that much of the vigorous hydrothermal circulation recorded in the Semail ophiolite was confined to the relatively permeable upper oceanic crust. However, the considerable areas of intense regional and localized actinolite alteration in the lower crust show that hydrothermal fluids, perhaps of a different nature, also circulated extensively through the lower-crustal gabbros. This is consistent with local outcrop and drillcore descriptions of hydrothermally altered gabbros and fault zones in the Semail lower crust (Coogan et al., 2006; Greenberger et al., 2021; Zihlmann et al., 2018), and reveals that these features are regionally prevalent and relevant at the crustal scale.

8. Conclusions

8.1. On the new Semail ophiolite alteration map

We have used ASTER L1T imagery, field mapping, and reflectance measurements to discriminate the spectrally similar alteration types epidosite, chlorite–epidote, actinolite, and serpentinite from regional spilite and lower crustal alteration across 4600 km^2 of the Semail ophiolite crustal outcrops. A preliminary map of regional versus undifferentiated localized alteration covers the remaining ~600 km^2 of crust along the W–SW inland flank of the Semail ophiolite, combining to a total map covering the entire 5100 km^2 of Semail ophiolite crustal outcrop.

The intensity multipliers for each classification qualitatively map out the intensity of alteration within these classified areas. Significantly, we were able to map SWIR absorption at ~2.34 μm, a proxy for the abundance of numerous common alteration minerals within the regional alteration. This regional alteration intensity map unveils the internal structure of by far the most voluminous domain of oceanic hydrothermal systems.

Together with its companion lithological map (Belgrano et al., 2019), our new alteration map should facilitate both novel scientific interpretation and mineral exploration of the fossil hydrothermal systems exposed in Earth's largest ophiolite. Our initial interpretation shows that while hydrothermal circulation leading to the formation of epidosites was largely confined to the upper oceanic crust, fluids also circulated both pervasively and along faults in the lower crust, leading to the formation of spatially variable regional alteration and structurally controlled actinolite alteration in the gabbros.

8.2. On multispectral discrimination of spectrally similar alteration minerals

Regional mapping of spectrally similar alteration minerals with multispectral data was not possible with established, generalized workflows. We accordingly developed several (pre-) processing optimizations specific to this task and study area. These included screening for scenes with residual atmospheric water features, normalizing the ASTER mosaic based on statistics from only the target areas, correcting across-mosaic ramp errors, and applying thresholds to the alteration classifications based on image data extracted over field-mapped reference areas (Fig. 3).

For the base imagery, we found the terrane correction of the ASTER L1T product to be advantageous over Level 2 reflectance products lacking precision terrane correction. For classification, the adaptable and transparent structure of LOAs (Mars and Rowan, 2006) proved to be effective in combining contextual and image-derived knowledge into reliable classifiers for the spectrally similar alteration types.

Despite the general success of our approach, chloritite alteration had a weak spectral response in the ASTER imagery and was often not distinguishable. With the exception of chlorite–epidote alteration, our classifications were also not able to differentiate sub-pixel mixtures of spectrally similar alteration minerals, and occasionally they over- or underestimate alteration intensity. These shortcomings are, to some extent, an inherent limitation of multispectral data (van der Meer et al., 2012), and new hyperspectral sensors should be capable of untangling such spectral mixtures.

Overall, the effectiveness of the workflow presented highlights the underappreciated potential of data-, site-, and target-specific optimization for geological remote sensing with ASTER, as opposed to direct reapplication of generalized methods. In doing so, we have produced high-resolution alteration maps of unprecedented scale for a mafic-dominated VMS district. Finally, this study underscores the continued value of constructing image processing workflows around field-based reference data and contextual knowledge. Despite the expense of field work, such an approach can evidently expand the utility of existing multispectral datasets.

Supplement and data archive

Both a Supplement and Data Archive are provided with this article. The supplement contains supporting tables and figures for this manuscript (Figs. S1–2; Tables S1–6). The data archive (https://doi.org/10.5281/zenodo.6565961) contains the final alteration map products and all the data and processing files required to reproduce and build on this work (Belgrano et al., 2022).

Credit author statement

Thomas Belgrano: Conceptualization, Methodology, Investigation, Analysis, Writing – Original Draft. Larryn Diamond: Conceptualization, Analysis, Supervision, Funding Acquisition, Writing - review & editing. Nevena Novakovic and Samuel Gilgen: Conceptualization, Methodology, Investigation, Analysis. Robert Hewson and Christoph Hecker: Investigation, Formal Analysis, Resources, Writing - review & editing. Robin Wolf, Ludwik de Doliwa Zieliński and Raphael Kuhn: Investigation, Formal Analysis.

Declaration of Competing Interest

The authors declare that they have no known competing financial interests or personal relationships that could have appeared to influence the work reported in this paper.

Data availability

All data and processing files required to reproduce and build on this work are archived at https://doi.org/10.5281/zenodo.6565961 (Belgrano et al., 2022)

Acknowledgments

The ASTER imagery used in this study was made available by NASA (USA) and METI (Japan), and NASA Land Processes Distributed Active Archive Center (LP DAAC) are thanked for data access. We thank the Ministry of Energy and Minerals (MEM), Sultanate of Oman, for their long support of this project, in particular Hussein Azubaibi, Mohammed Al Araimi, and Mohammed Al-Battashi. Khalid Al-Tobi and the team at National Earth Secrets Co. (Muscat) provided much appreciated logistical support. We thank Ali al Hashmi (MEM), Alannah Brett-Adams, Lisa Richter, Nicolas Zuluaga, Ivan Mercolli, Lea Weyermann, Fabian Scherer, and in particular, Samuel Weber (all University of Bern) for assistance during field mapping. The ITC, University of Twente facilitated spectroscopic measurements and Freek van der Meer, Frank van Ruitenbeek and colleagues are thanked for their advice. TMB acknowledges support from the SNSF and from the Southampton Marine and Maritime Institute, University of Southampton. This project was otherwise entirely funded by the University of Bern and by Swiss National Science Foundation (SNSF) Grant 200020-169653 to LWD.

Appendix A. Supplementary data

Supplementary data to this article can be found online at https://doi.org/10.1016/j.rse.2022.113211.

References

Abrams, M.J., Rothery, D.A., Pontual, A., 1988. Mapping in the Oman ophiolite using enhanced Landsat thematic mapper images. Tectonophysics 151, 387–401. https://doi.org/10.1016/0040-1951(88)90254-5.

Abweny, M.S., van Ruitenbeek, F.J.A., de Smeth, B., Woldai, T., van der Meer, F.D., Cudahy, T., Zegers, T., Blom, J.K., Thuss, B., 2016. Short-wavelength infrared

(SWIR) spectroscopy of low-grade metamorphic volcanic rocks of the Pilbara craton. J. Afr. Earth Sci. 117, 124–134. https://doi.org/10.1016/j.jafrearsci.2016.01.024.
Alabaster, T., Pearce, J.A., 1985. The interrelationship between magmatic and ore-forming hydrothermal processes in the Oman ophiolite. Econ. Geol. 80, 1–16. https://doi.org/10.2113/gsecongeo.80.1.1.
A'Shaikh, D., Matsueda, H., Mizuta, T., Miyashita, S., 2006. Hydrothermal alteration of Oman ophiolite extrusives in Ghuzayn area. Resour. Geol. 56, 167–182. https://doi.org/10.1111/j.1751-3928.2006.tb00277.x.
Barrie, C.T., Hannington, M.D., 1997. Classification of Volcanic-Associated Massive Sulfide Deposits Based on Host-Rock Composition. Volcanic Associated Massive Sulfide Deposits: Processes and Examples in Modern and Ancient Settings. https://doi.org/10.5382/Rev.08.01.
Belgrano, T.M., Diamond, L.W., 2019. Subduction-zone contributions to axial volcanism in the Oman-U.A.E. ophiolite. Lithosphere 11, 399–411. https://doi.org/10.1130/L1045.1.
Belgrano, T.M., Diamond, L.W., Vogt, Y., Biedermann, A.R., Gilgen, S.A., Al-Tobi, K., 2019. A revised map of volcanic units in the Oman ophiolite: insights into the architecture of an oceanic proto-arc volcanic sequence. Solid Earth 10, 1181–1217. https://doi.org/10.5194/se-10-1181-2019.
Belgrano, T.M., Diamond, L.W., Novakovic, N., Hewson, R.D., Hecker, C.A., Wolf, R.C., de Doliwa Zieliński, L., Kuhn, R., Gilgen, S.A., 2022. A 5000 km2 ASTER Alteration Map of the Oman–UAE Ophiolite Crust: Data Archive and Remote Sensing Toolkit. https://doi.org/10.5281/zenodo.6565961.
BME (Bishimetal Exploration), 1987. Geological Map of Al Wasit (Scale:1:50,000: Sheet NG40–14 E-III). Ministry of Petroleum and Minerals, Sultanate of Oman.
BRGM (Bureau de Recherches Geìologique et Minères), 1993. Geological Map of Fizh (Scale 1:50,000: Sheet NG40–14B4). Ministry of Petroleum and Minerals, Sultanate of Oman.
Charabi, Y., Al-Yahyai, S., 2013. Projection of future changes in rainfall and temperature patterns in Oman. J. Earth Sci. Clim. Chang. 2013, 1–8. https://doi.org/10.4172/2157-7617.1000154.
Coogan, L.A., Howard, K.A., Gillis, K.M., Bickle, M.J., Chapman, H., Boyce, A.J., Jenkin, G.R.T., Wilson, R.N., 2006. Chemical and thermal constraints on focussed fluid flow in the lower oceanic crust. Am. J. Sci. 306, 389–427. https://doi.org/10.2475/06.2006.01.
Cudahy, T., Shi, P., Novikova, Y., Fu, B., 2020. Satellite ASTER mineral mapping the provenance of the loess used by the ming to build their earthen Great Wall. Remote Sens. 12, 270. https://doi.org/10.3390/rs12020270.
Dalton, J.B., Bove, D.J., Mladinich, C.S., Rockwell, B.W., 2004. Identification of spectrally similar materials using the USGS Tetracorder algorithm: the calcite–epidote–chlorite problem. Remote Sens. Environ. 89, 455–466. https://doi.org/10.1016/j.rse.2003.11.011.
Du, Y., Cihlar, J., Beaubien, J., Latifovic, R., 2001. Radiometric normalization, compositing, and quality control for satellite high resolution image mosaics over large areas. IEEE Trans. Geosci. Remote Sens. 39, 623–634. https://doi.org/10.1109/36.911119.
Gilgen, S.A., Diamond, L.W., Mercolli, I., Al-Tobi, K., Maidment, D.W., Close, R., Al-Towaya, A., 2014. Volcanostratigraphic controls on the occurrence of massive sulfide deposits in the semail ophiolite, Oman. Econ. Geol. 109, 1585–1610. https://doi.org/10.2113/econgeo.109.6.1585.
Galley, A., Hannington, M., Jonasson, I., 2007. Volcanogenic Massive Sulphide Deposits. Geological Association of Canada, Mineral Deposits Division, Special Publication. https://doi.org/10.1016/0169-1368(95)00022-4.
Gilgen, S.A., Diamond, L.W., Mercolli, I., 2016. Sub-seafloor epidosite alteration: timing, depth and stratigraphic distribution in the Semail ophiolite, Oman. Lithos 260, 191–210. https://doi.org/10.1016/j.lithos.2016.05.014.
Goodenough, K.M., Styles, M.T., Schofield, D., Thomas, R.J., Crowley, Q.C., Lilly, R.M., McKervey, J., Stephenson, D., Carney, J.N., 2010. Architecture of the Oman–UAE ophiolite: evidence for a multi-phase magmatic history. Arab. J. Geosci. 3, 439–458. https://doi.org/10.1007/s12517-010-0177-3.
Greenberger, R.N., Harris, M., Ehlmann, B.L., Crotteau, M., Kelemen, P.B., Manning, C. E., Teagle, D.A.H., Team, the O.D.P.S, 2021. Hydrothermal alteration of the ocean crust and patterns in mineralization with depth as measured by micro-imaging infrared spectroscopy. J. Geophys. Res. Solid Earth. https://doi.org/10.1029/2021JB021976 n/a, e2021JB021976.
Hecker, C., Hook, S., van der Meijde, M., Bakker, W., van der Werff, H., Wilbrink, H., van Ruitenbeek, F., de Smeth, B., van der Meer, F., 2011. Thermal infrared spectrometer for earth science remote sensing applications-instrument modifications and measurement procedures. Sensors 11, 10981–10999. https://doi.org/10.3390/s111110981.
Hewson, R.D., Cudahy, T.J., Mizuhiko, S., Ueda, K., Mauger, A.J., 2005. Seamless geological map generation using ASTER in the Broken Hill-Curnamona province of Australia. Remote Sens. Environ. 99, 159–172. https://doi.org/10.1016/j.rse.2005.04.025.
Jowitt, S.M., McEvoy, F.M., Williamson, J.P., Bateson, L., Naden, J., Gunn, A.G., Nicolaides, S., 2005. In: Mao, J., Bierlein, F.P. (Eds.), Mineralisation Potential Mapping for Ophiolitehosted Volcanic Massive Sulphide (VHMS) Deposits, Troodos Ophiolite, Cyprus BT - Mineral Deposit Research: Meeting the Global Challenge. Springer Berlin Heidelberg, Berlin, Heidelberg, pp. 1469–1472. https://doi.org/10.1007/3-540-27946-6_373.
Kalinowski, A., Oliver, S., Aleks, K., Oliver, S., 2004. ASTER Mineral Index Processing Manual. Geoscience Australia.
Kelemen, P.B., Matter, J.M., Teagle, D.A.H., Coggon, J.A., 2020. Proceedings of the Oman Drilling Project. College Station, TX. Team, O.D.P.S. https://doi.org/10.14379/OmanDP.proc.2020.
Kokaly, R.F., Clark, R.N., Swayze, G.A., Livo, K.E., Hoefen, T.M., Pearson, N.C., Wise, R. A., Benzel, W.M., Lowers, H.A., Driscoll, R.L., Klein, A.J., 2017. USGS Spectral Library Version 7, Data Series. Reston, VA. https://doi.org/10.3133/ds1035.
Li, F., Jupp, D.L.B., Thankappan, M., Lymburner, L., Mueller, N., Lewis, A., Held, A., 2012. A physics-based atmospheric and BRDF correction for Landsat data over mountainous terrain. Remote Sens. Environ. 124, 756–770. https://doi.org/10.1016/j.rse.2012.06.018.
Lippard, S.J., Shelton, A.W., Gass, I.G., 1986. The Ophiolite of Northern Oman, Memoir (Geological Society of London). Blackwell Scientific Publications Ltd.
MacLeod, C.J., Johan Lissenberg, C., Bibby, L.E., 2013. "Moist MORB" axial magmatism in the Oman ophiolite: the evidence against a mid-ocean ridge origin. Geology 41, 459–462. https://doi.org/10.1130/G33904.1.
Mars, J.C., Rowan, L.C., 2006. Regional mapping of phyllic- and argillic-altered rocks in the Zagros magmatic arc, Iran, using advanced spaceborne thermal emission and reflection radiometer (ASTER) data and logical operator algorithms. Geosphere 2, 161–186. https://doi.org/10.1130/GES00044.1.
Mars, J.C., Rowan, L.C., 2010. Spectral assessment of new ASTER SWIR surface reflectance data products for spectroscopic mapping of rocks and minerals. Remote Sens. Environ. 114, 2011–2025. https://doi.org/10.1016/j.rse.2010.04.008.
Meyer, D., Siemonsma, D., Brooks, B., Johnson, L., 2015. Advanced Spaceborne Thermal Emission and Reflection Radiometer Level 1 Precision Terrain Corrected Registered at-Sensor Radiance (AST_L1T) Product, Algorithm Theoretical Basis Document. Open-File Report. Reston, VA. https://doi.org/10.3133/ofr20151171.
Miyashita, S., Adachi, Y., 2020. Chloritites from the Oman ophiolite: Possible roots of massive sulfide deposits. In: Nasir, S. (Ed.), Proceedings of the 2020 International Conference on Ophiolites and the Oceanic Lithosphere: Results of the Oman Drilling Project and Related Research. Sultan Qaboos University, Muscat, pp. 150–151.
NASA LP DAAC, 2015. ASTER Level 1 Precision Terrain Corrected Registered At-Sensor Radiance V003. https://doi.org/10.5067/ASTER/AST_L1T.003.
Nehlig, P., Juteau, T., 1988. Deep crustal seawater penetration and circulation at ocean ridges: evidence from the Oman ophiolite. Mar. Geol. 84, 209–228. https://doi.org/10.1016/0025-3227(88)90102-8.
Nicolas, A., Boudier, F., Ildefonse, B., Ball, E., 2000. Accretion of Oman and United Arab Emirates ophiolite – discussion of a new structural map. Mar. Geophys. Res. 21, 147–180. https://doi.org/10.1023/A:1026769727917.
Pflumio, C., 1991. Evidences for Polyphased Oceanic Alteration of the Extrusive Sequence of the Semail Ophiolite from the Salahi Block (Northern Oman). Ophiolite Genesis and Evolution of the Oceanic Lithosphere, 5, pp. 313–351. https://doi.org/10.1007/978-94-011-3358-6_17.
Rajendran, S., Nasir, S., 2017. Characterization of ASTER spectral bands for mapping of alteration zones of volcanogenic massive sulphide deposits. Ore Geol. Rev. https://doi.org/10.1016/j.oregeorev.2017.04.016.
Rajendran, S., Nasir, S., 2019. ASTER capability in mapping of mineral resources of arid region: a review on mapping of mineral resources of the Sultanate of Oman. Ore Geol. Rev. 108, 33–53. https://doi.org/10.1016/j.oregeorev.2018.04.014.
Rothery, D.A., 1984. The role of Landsat multispectral scanner (MSS) imagery in mapping the Oman ophiolite. Geol. Soc. Spec. Publ. https://doi.org/10.1144/GSL.SP.1984.013.01.33.
Rowan, L.C., Mars, J.C., 2003. Lithologic mapping in the mountain pass, California area using advanced spaceborne thermal emission and reflection radiometer (ASTER) data. Remote Sens. Environ. 84, 350–366. https://doi.org/10.1016/S0034-4257(02)00127-X.
Roy, R., Launeau, P., Carrère, V., Pinet, P., Ceuleneer, G., Clénet, H., Daydou, Y., Girardeau, J., Amri, I., 2009. Geological mapping strategy using visible near-infrared-shortwave infrared hyperspectral remote sensing: application to the Oman ophiolite (Sumail Massif). Geochem. Geophys. Geosyst. 10, n/a–n/a. https://doi.org/10.1029/2008GC002154.
Sivitskis, A.J., Harrower, M.J., David-Cuny, H., Dumitru, I.A., Nathan, S., Wiig, F., Viete, D.R., Lewis, K.W., Taylor, A.K., Dollarhide, E.N., Zaitchik, B., Al-Jabri, S., Livi, K.J.T., Braun, A., 2018. Hyperspectral satellite imagery detection of ancient raw material sources: soft-stone vessel production at Aqir al-Shamoos (Oman). Archaeol. Prospect. 25, 363–374. https://doi.org/10.1002/arp.1719.
Smith, G.M., Milton, E.J., 1999. The use of the empirical line method to calibrate remotely sensed data to reflectance. Int. J. Remote Sens. 20, 2653–2662. https://doi.org/10.1080/014311699211994.
Stakes, D.S., Taylor, H.P., 1992. The northern Samail ophiolite: an oxygen isotope, microprobe, and field study. J. Geophys. Res. https://doi.org/10.1029/91JB02743.
van der Meer, F.D., van der Werff, H.M.A., van Ruitenbeek, F.J.A., Hecker, C.A., Bakker, W.H., Noomen, M.F., van der Meijde, M., Carranza, E.J.M., de Smeth, J.B., Woldai, T., 2012. Multi- and hyperspectral geologic remote sensing: a review. Int. J. Appl. Earth Obs. Geoinf. https://doi.org/10.1016/j.jag.2011.08.002.
Weber, S., Diamond, L.W., Alt-Epping, P., Brett-Adams, A.C., 2021. Reaction mechanism and water/rock ratios involved in epidosite alteration of the oceanic crust. J. Geophys. Res. Solid Earth 126. https://doi.org/10.1029/2020JB021540 e2020JB021540.
White, A.J.R., Laukamp, C., Stokes, M.A., Legras, M., Pejcic, B., 2017. Vibrational spectroscopy of epidote, pumpellyite and prehnite applied to low-grade regional metabasites. Geochemistry. https://doi.org/10.1144/geochem2016-007.
Yoshitake, N., Arai, S., Ishida, Y., Tamura, A., 2009. Geochemical characteristics of chloritization of mafic crust from the northern Oman ophiolite: implications for estimating the chemical budget of hydrothermal alteration of the oceanic lithosphere. J. Mineral. Petrol. Sci. https://doi.org/10.2465/jmps.081022b.
Zihlmann, B., Müller, S., Coggon, R.M., Koepke, J., Garbe-Schönberg, D., Teagle, D.A.H., 2018. Hydrothermal fault zones in the lower oceanic crust: an example from Wadi Gideah, Samail ophiolite, Oman. Lithos 323, 103–124. https://doi.org/10.1016/j.lithos.2018.09.008.